Cell Reports

Article

PIEZO1-dependent mode switch of neuronal migration in heterogeneous microenvironments in the developing brain

Graphical abstract

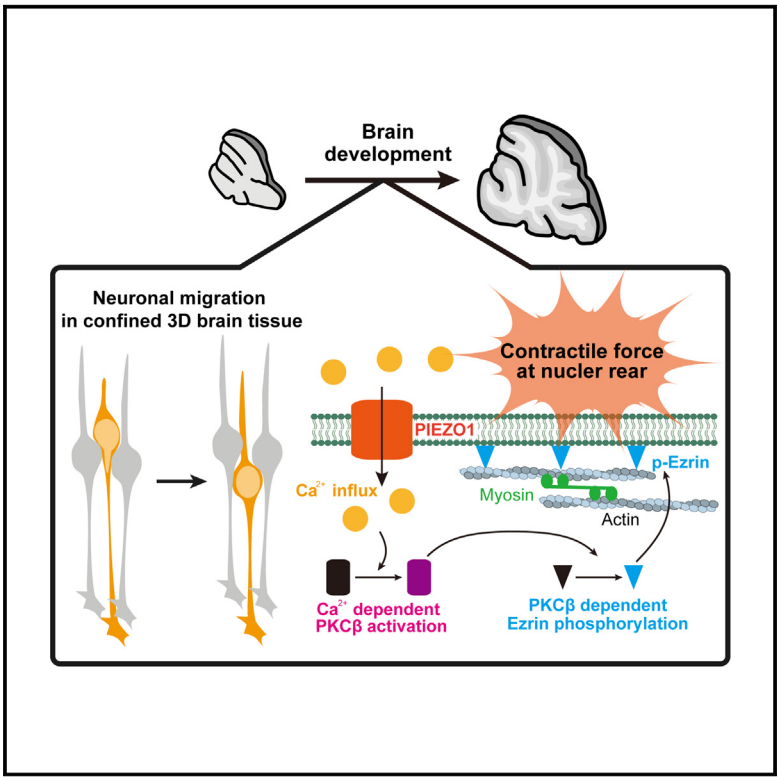

Highlights

- Neurons switch migration modes in 2D and 3D environments
- PIEZO1 is activated in 3D confined space and induces Ca^{2+} influx
- Ca^{2+}-dependent PKC translocates ezrin and actomyosin to the posterior membrane
- Actomyosin generates contractile forces posteriorly during migration in 3D spaces

Authors

Naotaka Nakazawa, Gianluca Grenci, Yoshitaka Kameo, ..., Taiji Adachi, Keiko Nonomura, Mineko Kengaku

Correspondence

nakazawa.naotaka@emat.kindai.ac.jp (N.N.), kengaku@icems.kyoto-u.ac.jp (M.K.)

In brief

Nakazawa et al. show that the cerebellar granule cell is equipped with multiple actomyosin engines to migrate in the heterogeneous microenvironment of developing brain tissue. In a 3D confined environment, PIEZO1 induces the translocation of actomyosin to the posterior membrane through PKC-ezrin signaling and generates pushing force in the migrating neuron.

Nakazawa et al., 2025, Cell Reports *44*, 115405
March 25, 2025
https://doi.org/10.1016/j.celrep.2025.115405

CellPress

Cell Reports

CellPress
OPEN ACCESS

Article

PIEZO1-dependent mode switch of neuronal migration in heterogeneous microenvironments in the developing brain

Naotaka Nakazawa,[1,2,11,*] Gianluca Grenci,[3,4] Yoshitaka Kameo,[5,6,7,10] Noriko Takeda,[1,5] Tsuyoshi Sawada,[6,7] Junko Kurisu,[1] Zhejing Zhang,[1,5] Kenichi Toma,[1] Taiji Adachi,[1,5,6,7] Keiko Nonomura,[5,8,9] and Mineko Kengaku[1,5,*]

[1]Institute for Integrated Cell-Material Sciences (KUIAS-iCeMS), Kyoto University, Kyoto 606-8501, Japan
[2]Faculty of Science and Engineering, Kindai University, Osaka 577-8502, Japan
[3]Mechanobiology Institute, National University of Singapore, Singapore 117411, Singapore
[4]Biomedical Engineering Department, National University of Singapore, Singapore 117583, Singapore
[5]Graduate School of Biostudies, Kyoto University, Kyoto 606-8501, Japan
[6]Institute for Life and Medical Sciences, Kyoto University, Kyoto 606-8501, Japan
[7]Graduate School of Engineering, Kyoto University, Kyoto 615-8530, Japan
[8]Department of Life Science and Technology, Tokyo Institute of Technology, Kanagawa 226-8501, Japan
[9]National Institute for Basic Biology, Aichi 444-8585, Japan
[10]College of Engineering, Shibaura Institute of Technology, Tokyo 135-8548, Japan
[11]Lead contact
*Correspondence: nakazawa.naotaka@emat.kindai.ac.jp (N.N.), kengaku@icems.kyoto-u.ac.jp (M.K.)
https://doi.org/10.1016/j.celrep.2025.115405

SUMMARY

The migration of newborn neurons is essential for brain morphogenesis and circuit formation, yet controversy exists regarding how neurons generate the driving force against strong mechanical stresses in crowded neural tissues. We found that cerebellar granule neurons employ a mechanosensing mechanism to switch the driving forces to maneuver in irregular brain tissue. In two-dimensional (2D) cultures, actomyosin is enriched in the leading process, exerting traction force on the cell soma. In tissue or 3D confinement, however, actomyosin concentrates at the posterior cell membrane, generating contractile forces that assist passage through narrow spaces, working alongside the traction force in the leading process. The 3D migration is initiated by the activation of a mechanosensitive channel, PIEZO1. PIEZO1-induced calcium influx in the soma triggers the PKC-ezrin cascade, which recruits actomyosin and transmits its contractile force to the posterior plasma membrane. Thus, migrating neurons adapt their motility modes in distinct extracellular environments in the developing brain.

INTRODUCTION

Cell migration is important in various physiological and pathological events, such as morphogenesis, immune surveillance, and cancer metastasis. On two-dimensional (2D) substrates, cell migration is driven by the propulsive force of polymerizing cortical actin that is anchored to transmembrane adhesion receptors in the leading edge.[1–3] However, recent studies have revealed that cells confined in 3D matrices can adopt multiple motility modes based on the physical environment, availability of cell-matrix adhesion, and effective sites for actomyosin contraction.[4–6] The mechanism of 3D migration has been intensively studied using mesenchymal cancer cells,[7–10] germ cells,[11,12] fibroblasts,[13,14] and immune cells,[15–17] mostly in cultured conditions, but has yet to be identified under *in vivo* conditions and in other migratory cell types, including neural cells in the brain.

Postmitotic neurons in the mammalian brain migrate long distances during cortical brain development. Migrating neurons typically extend a long leading process and translocate the cell soma, including the nucleus, into the leading process. In these cells, force generation and transmission also rely on actomyosin dynamics, in addition to the steering force of perinuclear microtubules and their motor proteins.[18,19] However, considerable diversity in actomyosin force generation has been found in different models of neuronal migration. For instance, in migrating forebrain interneurons in organotypic slices or Matrigel, nonmuscle myosin II (hereafter called myosin) is enriched at the rear of the cell and exerts a pushing force behind the nucleus.[20–24] In contrast, in migrating cerebellar granule neurons (CGNs) on culture dishes coated with extracellular matrix (ECM), actomyosin in the leading process generates an adhesion-dependent traction force that pulls the nucleus along with the perinuclear microtubules in the cell soma.[25–28] The controversy over whether the actomyosin force is generated in the front or the rear has been attributed to the differences in neuron types and assay systems.[19,29,30]

In this study, we investigated actomyosin dynamics during neuronal migration in different extracellular environments using

CGNs as a model. We found that actomyosin dynamically changes its subcellular localization within the same cell, depending on the 2D and 3D extracellular environments, and generates an effective driving force for neuronal migration. We demonstrate that a migrating neuron is not governed by a single migratory mode but is equipped with multiple engines and can switch between driving forces via a mechanosensor PIEZO1.

RESULTS

Neurons hire differential actomyosin forces in 2D and 3D environments

During the formation of the cerebellar cortex, CGNs born in the external granular layer (EGL) migrate in the molecular layer (ML) to the internal granular layer (IGL). We and others have reported that CGNs migrate by the traction force of actomyosin enriched in the leading process using dissociated cultures on laminin-coated dishes.[25–28] To investigate whether CGNs in developing brain tissue adopt the same mechanism by which the soma is ''pulled'' by the traction force in the leading process, we monitored actomyosin dynamics in an organotypic cerebellar slice culture.[31,32] We electroporated GFP-tagged myosin regulatory light chain (MRLC-2GFP) into immature CGNs in the neonatal mouse cerebellum and observed myosin dynamics in migrating CGNs in the organotypic culture (Figure 1A). CGNs underwent typical saltatory movements with intermittent forward displacement of the soma.[31] Unlike CGNs in 2D culture, where actomyosin is enriched in the leading process, myosin distribution was broader and dynamically changed in the cell soma (Figures 1A and 1B). Moreover, in many cases, it appeared to localize at the rear of the soma prior to a large-amplitude saltatory movement (Figures 1B–1D, S1A, and S1B; Video S1).

To ask whether the environment in which CGNs are situated influences actomyosin dynamics, we next observed the migration of CGNs embedded within 3D Matrigel or plated on its surface (Figure 1E). In neurons cultured on the Matrigel surface, myosin localized to the cell front and leading process, as was previously observed on 2D substrates (Figures 1F–1H; Video S2).[25,27,28] In contrast, in neurons embedded in Matrigel, myosin appeared more dynamic and frequently enriched at the rear of the cell, as in the cerebellar tissue in slice cultures (Figures 1I–1K; Video S2). Actomyosin was also enriched in the growth cone, which generates propulsive force for axon extension. There was no striking difference in actomyosin distribution in the growth cone under 2D and 3D conditions (Figure S1C; Video S2). We also monitored microtubule dynamics and found no obvious change in 2D and 3D cultures (Figure S1D; Video S3). These results suggest that actomyosin localization in the soma and the proximal leading process of migrating CGNs are differentially regulated in 2D and 3D extracellular environments.

We then tested whether such a mode transition is fundamental among neuronal types by examining cortical interneurons (Figure S1E). In dissociated interneurons in 3D Matrigel, myosin was highly enriched in the rear of the cell, consistent with previous reports.[20–23] In contrast, on the Matrigel surface, myosin did not clearly localize in the rear but instead was more broadly distributed in the neurons (Figure S1F). Thus, at least two different types of neurons change actomyosin localization depending on the extracellular environment.

To further characterize neuronal migration in a 3D environment, we designed micropatterned channels connected by narrow tunnels that mimic confined extracellular spaces in brain tissues (Figures 2A and S2A). Dissociated CGNs were capable of passing through tunnels with a width of 3 μm (5 μm height), much smaller than the CGN somal diameter of about 6 μm (Figures 2B and S2B; Video S4). Myosin dynamically moved throughout the entire cell soma in neurons situated in a wide channel. When these cells migrated into a narrow tunnel, myosin localized at the rear periphery of the cell until the entire cell soma passed through the tunnel into the next channel (Figure S2C). During the passage of the cell soma through the tunnel, we observed that transient membrane blebs actively formed at the actin-rich cell rear, implying actomyosin contractility at the posterior plasma membrane[33] (Figure 2C; Video S4). These results suggest that neurons localize actomyosin at the rear plasma membrane to exert a contractile force, assisting the passage through a narrow constriction.

We next performed a computational simulation to verify whether actomyosin contractility in the cell rear is effective in confined migration. We assumed that a cell resembles a deformable and slightly compressible spherical object covered with a hyperelastic membrane (Table S4). The model cell entered a narrow tunnel by tensile force on the front membrane with or without the contraction at the rear edge. With only the front force, the cell deformed and moved forward until the front edge entered the constriction, but the rear half stopped at the constriction. In contrast, when the contraction of the membrane at the rear edge was combined with the front force, the entire cell successfully entered and passed through the narrow tunnel (Figure 2D; Video S5). Collectively, the simulation results suggest that actomyosin contraction at the cell rear can produce forward propulsion that enables neurons to pass through narrow constrictions.

PIEZO1 in CGNs is essential for migration in 3D confinement

In order to identify the mechanism regulating the posterior localization and contraction of actomyosin in a confined microenvironment, we performed a pharmacological screen in a transwell assay where cells migrate through polycarbonate membranes with different pore sizes (Figure 3A).[34] The majority of CGNs seeded on the membranes underwent transwell migration through both confined 3-μm pores (67% at 6 h) and permissive 8-μm pores (85% at 6 h) (Figures S3A and S3B). The inhibition of actin turnover (cytochalasin D, latrunculin B, or jasplakinolide) or myosin activity (blebbistatin) strongly reduced transmigration through both 3- and 8-μm pores, supporting the notion that actomyosin dynamics is indispensable for neuronal migration in both confined and non-confined spaces (Figure 3B). Among a set of molecules tested under confined and non-confined conditions, we found that treatment with GsMTx4, a peptide inhibitor of mechanosensitive ion channels (MSCs), specifically reduced transmigration of CGNs through 3-μm pores but not 8-μm pores (Figure 3C).[35,36] As GsMTx4 inhibits both transient receptor potential (TRP; except for TRPV4) and PIEZO families, we asked which class of MSCs was responsible for confined

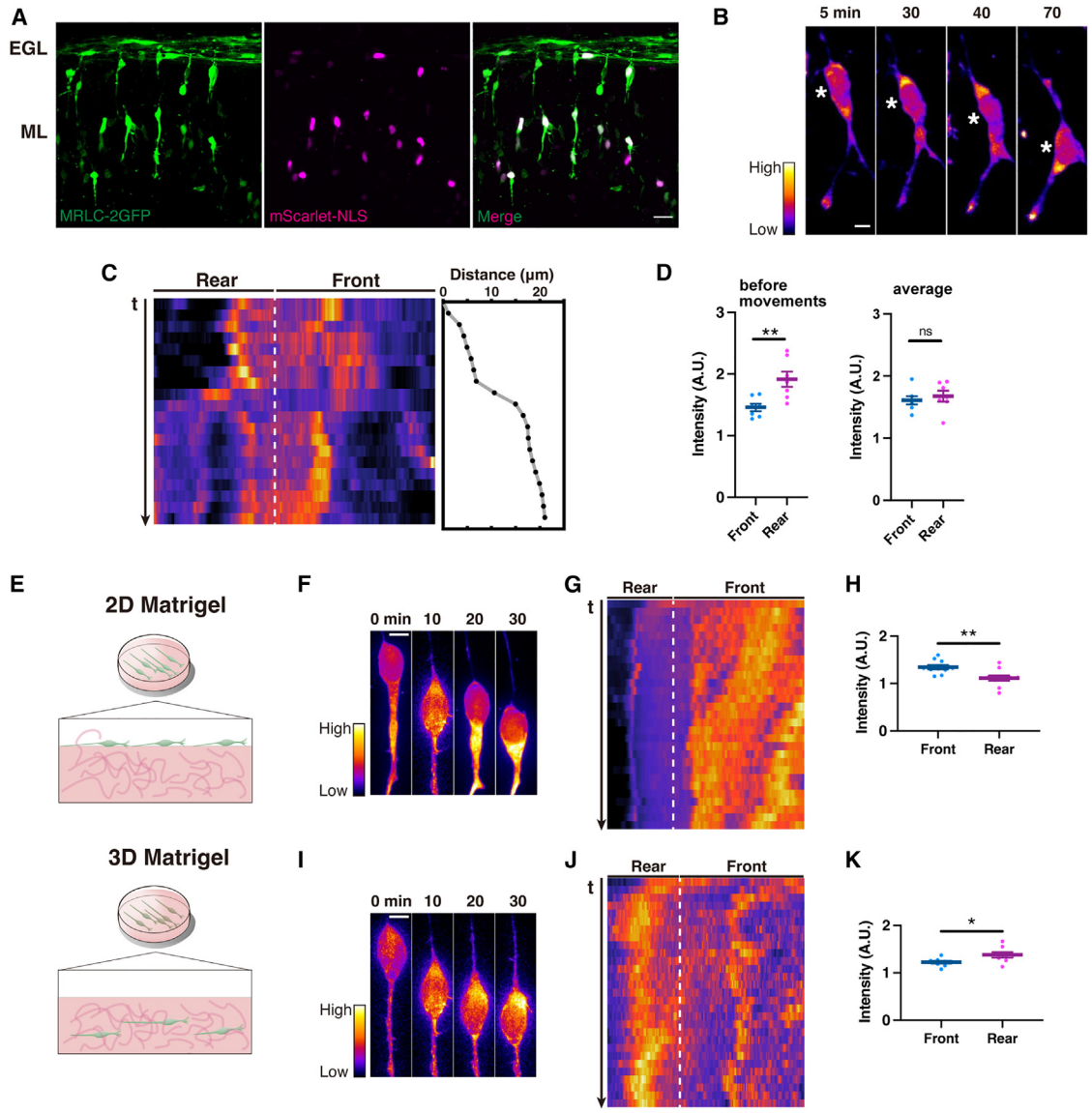

Figure 1. Actomyosin is differentially localized in 2D and 3D microenvironments

(A) Snapshot image of CGNs electroporated with MRLC-2GFP (green) and mScarlet-NLS (magenta) in cerebellar tissue isolated from P10 mouse. EGL, external granule layer; ML, molecular layer.

(B) Image sequence of a CGN migrating in the ML in the cerebellar slice.

(C) Heatmap display of the relative (rear/front) distribution of myosin (MRLC-2GFP) to the nucleus (dashed line indicates the nuclear center) in the neuron shown in (B) plotted against time. Nuclear displacement in the ML toward the IGL is plotted on the right.

(D) The rear/front distribution of myosin in migrating CGNs in slice cultures prior to a large-amplitude movement of the soma (left) or averaged over 120 min (right). $n = 7$ neurons.

(E) 2D and 3D CGN cultures.

(F–H) Image sequence (F), time-dependent change in myosin localization (G), and the rear/front comparison of averaged myosin localization (H) in migrating CGNs in 2D Matrigel culture. $n = 10$ neurons.

(I–K) Image sequence (I), time-dependent change in myosin localization (J), and the rear/front comparison of averaged myosin localization (K) in migrating CGNs in 3D Matrigel culture. $n = 8$ neurons.

Samples were collected from three independent experiments in (D), (H), and (K). $^{*}p < 0.05$ and $^{**}p < 0.01$, Mann-Whitney test. Data are represented as mean ± SEM. Scale bars, 20 μm (A) and 5 μm (B, F, and I).

migration.[37] Among potential mechanosensing TRP channels, inhibition of TRPC and TRPV channels by SKF96365 or the TRPV4 channel by HC-067047 had no overt differential effects on migration through 3- and 8-μm pores (Figure 3D).[38,39] In contrast, conditional deletion of PIEZO1 in CGNs (NeuroD1-Cre; Piezo1$^{flox/flox}$, hereafter called PIEZO1 cKO [conditional

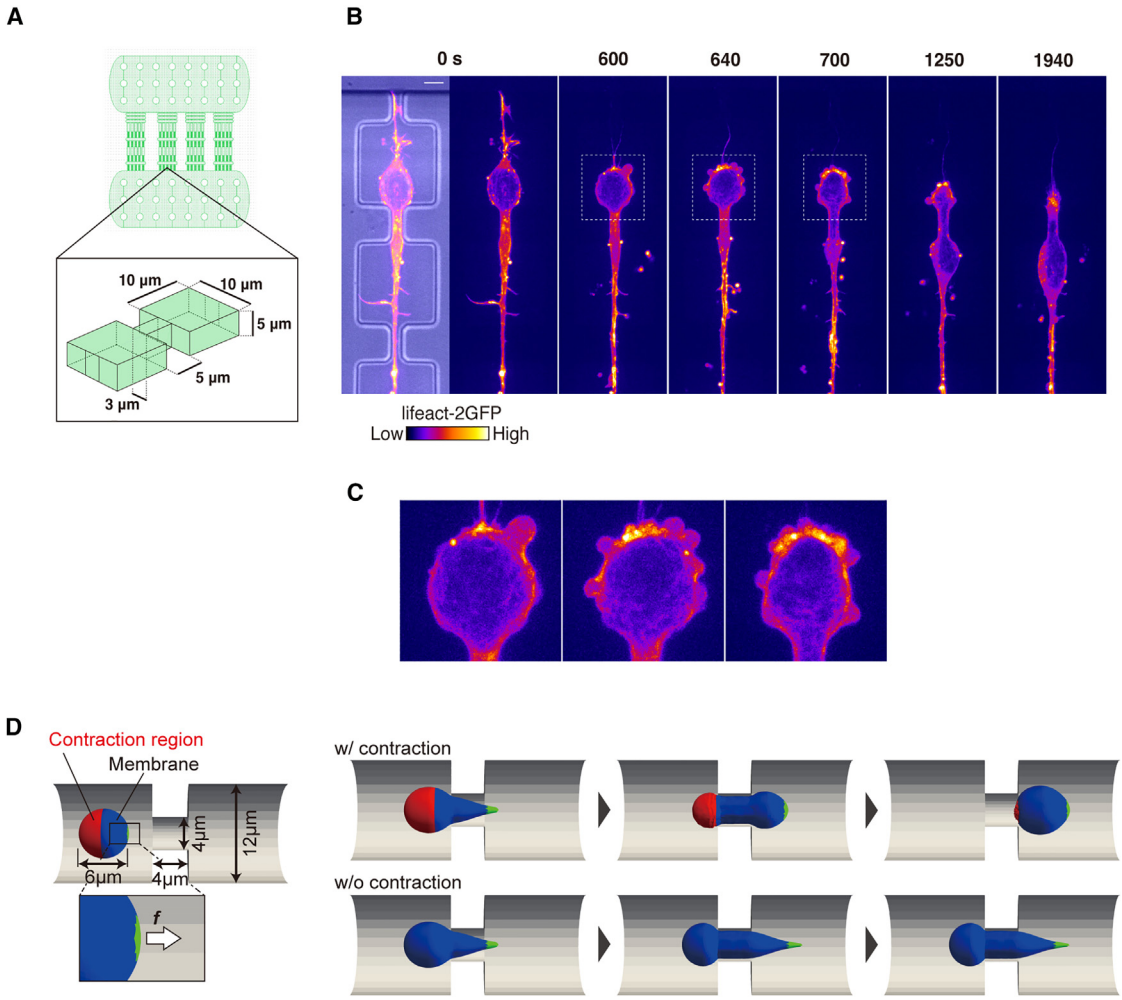

Figure 2. Actomyosin contraction in the rear plasma membrane in CGNs migrating in confined spaces

(A) Micropatterned substrates with repetitive constrictions.

(B) Image sequence of a CGN transfected with lifeact-2GFP moving through 3 × 5 × 5 μm^3 constrictions (right 6 images). Scale bar, 5 μm.

(C) Magnified view of the CGN in (B) at 600, 640, and 700 s.

(D) Simulation of a deformable spherical object that moves into a narrow tunnel. The red color indicates the area where contraction occurs, and the green color indicates the area where tensile force is applied.

See also Figure S2 and Videos S4 and S5.

knockout]) strongly reduced transwell migration through 3-μm pores but had little effect on migration through 8-μm pores (Figure 3E).[40] These results suggest that mechanical stress during penetration into the narrow pores activates PIEZO1 and evokes the molecular signal necessary for confined migration.

PIEZO1 mRNA expression in developing CGNs was confirmed by RNAscope *in situ* hybridization and RNA sequencing (RNA-seq) analysis (Figures S3D and S3E; Tables S1 and S2). We also monitored PIEZO1 protein localization in CGNs isolated from PIEZO1-tdTomato knockin mice. PIEZO1 was distributed in punctate patterns along the entire cell soma and leading process, in agreement with previous reports using frog retinal neurons (Figure 3F).[41,42] There was no apparent difference in PIEZO1 localization in 2D and 3D environments, suggesting that PIEZO1 is constitutively expressed in migrating CGNs.

We next examined PIEZO1 activity in CGNs by applying a specific agonist, Yoda1, in a dissociated culture.[43] In the presence of external Ca^{2+} (1.8 mM), Yoda1 treatment induced a slow and prolonged increase in the intracellular Ca^{2+} concentration ($[Ca^{2+}]_i$) in the entire cell as visualized by a GCaMP6s probe (Figure 3G; Video S6).[44] The increase in $[Ca^{2+}]_i$ by Yoda1 treatment was inhibited by the selective PIEZO1 inhibitor Dooku1 or a membrane-impermeable extracellular Ca^{2+} chelator, BAPTA, indicating that the activated PIEZO1 allows Ca^{2+} entry into the CGN cytoplasm (Figures 3G–3I).

Previous studies have shown that PIEZO1 localizes to both the plasma membrane and the endoplasmic reticulum (ER) and mediates Ca^{2+} release from the ER as well as the influx of extracellular Ca^{2+}.[45,46] To identify the source of the $[Ca^{2+}]_i$ increase induced by Yoda1, we pretreated the CGNs with an ER Ca^{2+}-ATPase blocker,

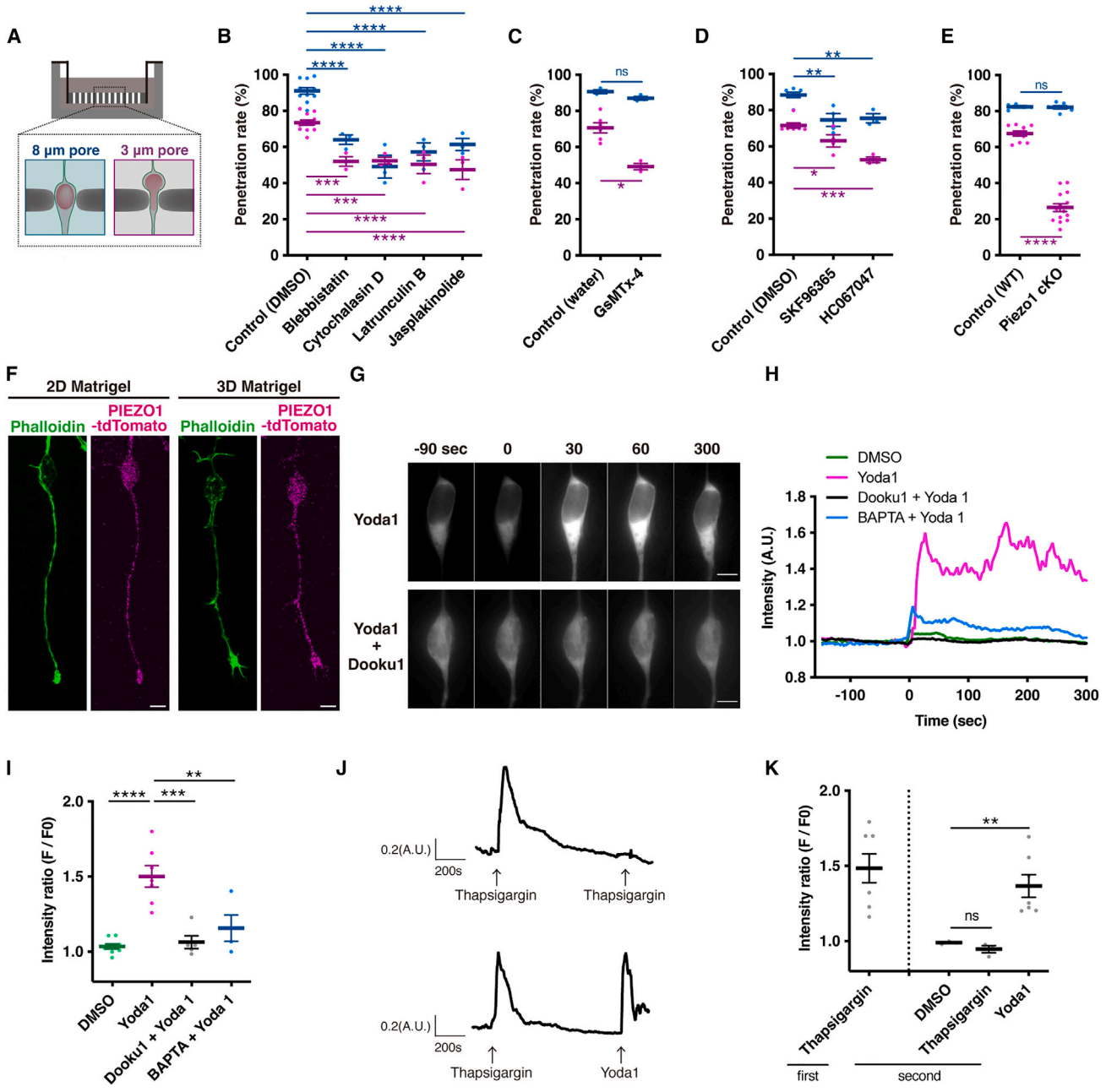

Figure 3. PIEZO1 is active in migrating CGNs

(A) Transwell assay.

(B) Treatment with inhibitors of actomyosin dynamics. Drugs were added 2 h after seeding dissociated CGNs in transwell dishes. The percentages of cells that migrated to the bottom side through 3-μm (purple) or 8-μm (blue) pores (penetration rates) were calculated. $n \geq 150$ neurons per condition.

(C–E) The effects of a mechanosensitive channel blocker GsMTx4 (C), TRP channel inhibitors (D), and conditional deletion of PIEZO1 (E). $n \geq 150$ neurons per condition.

(F) PIEZO1 protein localization in 2D and 3D cultures. The CGNs were isolated from PIEZO1-tdTomato mice. Scale bars, 5 μm.

(G) Ca^{2+} elevation in cultured CGNs treated with Yoda1 (100 μM) with or without its antagonist Dooku1 (100 μM). Drugs were added at time 0. Scale bars, 5 μm.

(H) The GCAMP6s ΔF/F transients in the soma upon treatment with Yoda1 in the presence or absence of Dooku1 or BAPTA (2-[2-[2-[2-[Bis(carboxymethyl)amino] phenoxy]ethoxy]-N-(carboxymethyl)anilino]acetic acid).

(I) Mean ratio of peak amplitudes of GCAMP6s ΔF/F transients. $n \geq 3$ neurons per condition.

(J) Ca^{2+} elevation evoked by 2 treatments with thapsigargin (top) and a treatment with thapsigargin followed by Yoda1 (bottom).

(K) Mean ratio of peak amplitudes of GCAMP6s ΔF/F transients. $n \geq 3$ neurons per condition.

Samples were collected from three independent experiments. $^{*}p < 0.05$, $^{**}p < 0.01$, $^{***}p < 0.001$, and $^{****}p < 0.0001$. One-way ANOVA in (B), (D), (H), and (J). Mann-Whitney test in (C) and (E). Data are represented as mean ± SEM. See also Figure S3 and Videos S6 and S7.

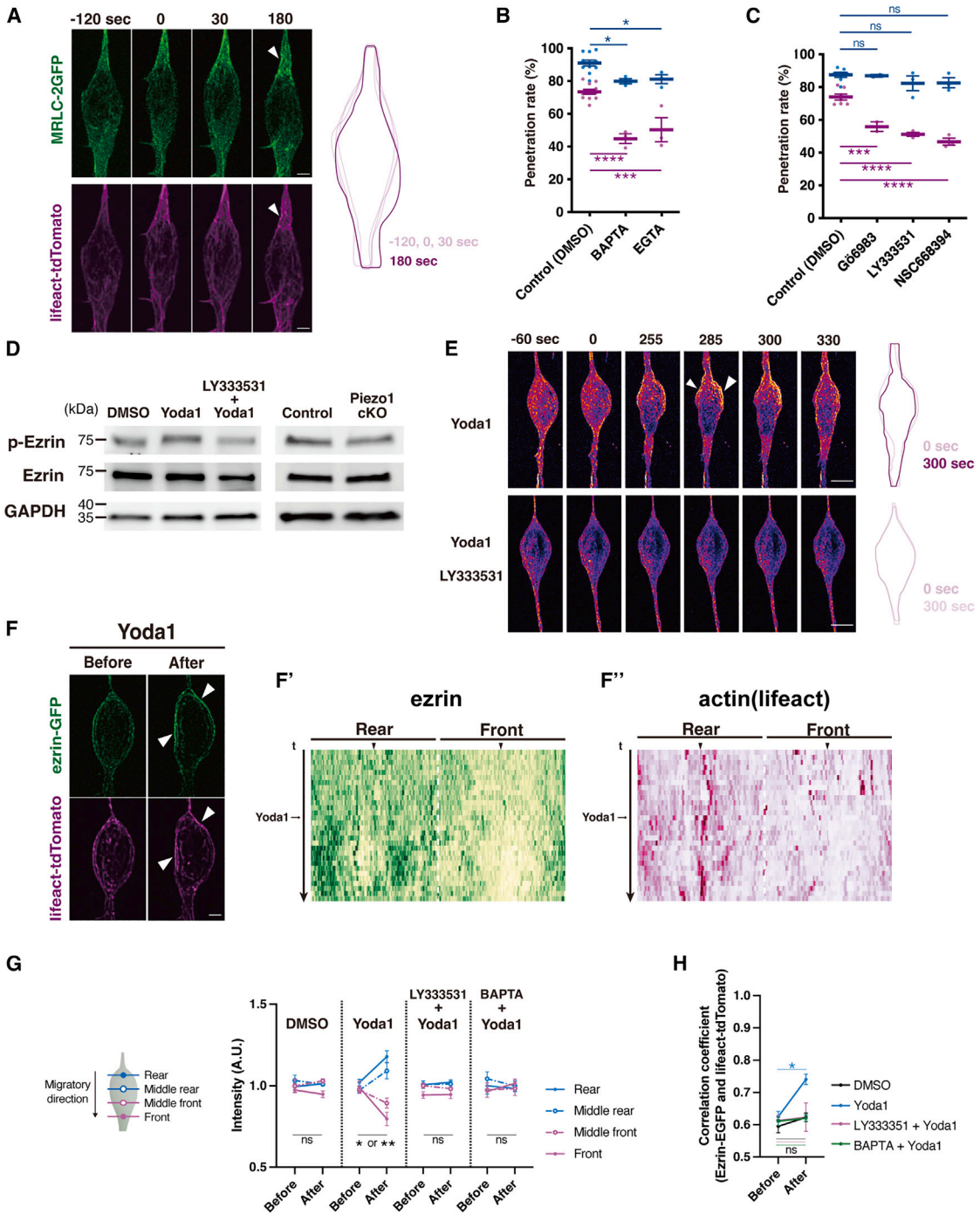

Figure 4. PIEZO1 induces plasma membrane recruitment of actomyosin via the PKC-ezrin pathway

(A) Left, time-lapse sequence of MRLC-2GFP and lifeact-tdTomato signals in CGNs upon Yoda1 treatment. Arrowheads indicate strong accumulation of MRLC and lifeact signals. Right, colored outlines mark the periphery of the soma at various time points.

(B and C) Percentages of cells that passed through 3- or 8-μm transwell pores in the presence of Ca^{2+}chelators (B) and inhibitors of Ca^{2+}-dependent PKCs or ezrin (C). $n \geq 150$ neurons per condition. Samples were collected from more than three independent experiments. $^{*}p < 0.05$, $^{***}p < 0.001$, and $^{****}p < 0.0001$, one-way ANOVA.

(D) Phosphorylation and activation of ezrin in CGNs treated with Yoda1 with or without LY333531 (left) and CGNs from wild-type and PIEZO1 cKO mice (right). Western blotting was performed with antibodies against phospho-T576 ezrin (p-Ezrin), total ezrin (Ezrin), and GAPDH.

(E) Time-lapse sequence of ezrin-GFP signals in CGNs upon treatment with Yoda1 (left). Cells were pretreated with or without LY333531. Arrowheads indicate strong accumulation of ezrin signals. Traces at the right are shape changes of the soma after Yoda1 treatment.

(legend continued on next page)

thapsigargin, to exhaust the ER Ca^{2+} store before the addition of Yoda1. Thapsigargin pretreatment induced a transient $[Ca^{2+}]_i$ rise, while the second thapsigargin administration at 15 min caused little or no response in the same cell, confirming that the pretreatment depleted Ca^{2+} from the ER (Figures 3J, top, and 3K). In contrast, Yoda1 treatment at 15 min after the thapsigargin pretreatment induced a large $[Ca^{2+}]_i$ elevation, indicating that PIEZO1 induces the bulk of the Ca^{2+} influx from the extracellular environment (Figures 3J, bottom, and 3K).

To further demonstrate the involvement of PIEZO1 in 3D confined migration, we monitored Ca^{2+} dynamics in CGNs migrating in 2D and 3D cultures. We observed fluctuation of $[Ca^{2+}]_i$ in the soma of CGNs migrating in 2D culture, in agreement with previous reports.[47] In contrast, CGNs migrating in 3D culture showed Ca^{2+} influxes with greater amplitudes (Figures S3F and S3G; Video S7). Conversely, CGNs from PIEZO1-deficient mice exhibited no significant difference in Ca^{2+} dynamics between 2D and 3D conditions (Figures S3F and S3G; Video S7). These results support that CGNs undergo PIEZO1-induced Ca^{2+} influx in 3D confinement. Taken together, these results suggest that CGNs express PIEZO1 in the plasma membrane and undergo Ca^{2+} influx upon PIEZO1 activation by passage through narrow spaces.

PIEZO1 signaling triggers actomyosin force transmission in 3D confinement

Notably, the Yoda1-induced Ca^{2+} elevation was followed by the surface accumulation of actomyosin and twitching of the cell soma, suggesting that the activation of PIEZO1 induced actomyosin translocation to the plasma membrane (Figure 4A; Video S8). We, therefore, sought to identify the signaling pathway downstream of PIEZO1 by drug screening in the transwell assay. We first confirmed that BAPTA or EGTA treatment attenuated migration through 3-μm pores and, more weakly, 8-μm pores (Figure 4B). Among multiple candidates of downstream effectors, we found that pharmacological inhibition of Ca^{2+}-dependent protein kinase C (PKC; PKCα, -β, and -γ) by Gö6983 produced differential effects on migration through 3- and 8-μm pores (Figure 4C). Inhibition of PKCβ, the most abundant Ca^{2+}-dependent PKC in CGNs (Table S3), by LY333531 was sufficient to suppress confined migration through 3-μm pores. Furthermore, inhibition of ezrin by NSC668394 also specifically attenuated confined migration through 3-μm pores.

It has been shown that ezrin is activated upon phosphorylation at threonine 567 (T567) by Ca^{2+}-dependent PKCs.[48–50] To further confirm the involvement of PKC and ezrin in PIEZO1 signaling, we analyzed ezrin phosphorylation in PIEZO1-activated and non-activated CGNs. Indeed, PIEZO1 activation by Yoda1 treatment significantly elevated the phosphorylation of ezrin T567, which was inhibited by preincubation with PKCβ inhibitor LY333531 (Figures 4D, left, and S4A). Furthermore, the basal level of ezrin phosphorylation was downregulated in CGNs from PIEZO1 cKO mice (Figures 4D, right, and S4B). These results suggest that PIEZO1-induced Ca^{2+} influx activates Ca^{2+}-dependent PKCβ, which in turn phosphorylates ezrin in CGNs.

The ERM (ezrin-radixin-moesin) proteins translocate to the plasma membrane upon phosphorylation and tether the actin cytoskeleton to the plasma membrane.[51,52] We hypothesized that Ca^{2+} signaling induced by PIEZO1 leads to the activation and translocation of ezrin and actomyosin to the plasma membrane, inducing contraction of the cell soma. Indeed, ezrin translocated at the posterior periphery of the cell when the cell soma entered the tunnel of micropatterned channels (Figure S4C). Furthermore, we observed that Yoda1 treatment of dissociated CGNs induced significant translocation of ezrin-GFP to the plasma membrane at the cell rear, followed by somal twitching (Figure 4E; Video S9). Strikingly, actin filaments visualized by life-act-tdTomato were recruited at the sites of ezrin-GFP localization upon Yoda1 treatment (Figures 4F–4F″). Pretreatment with BAPTA or LY333531 abolished not only the translocation of ezrin and actin but also cell soma twitching in response to Yoda1 treatment (Figures 4E, 4G, 4H, S4D–4D‴, and S4E–4E‴; Videos S9 and S10). These data strongly suggest that PIEZO1-mediated Ca^{2+} influx facilitates actomyosin force transmission at the posterior cell membrane through activation of the PKCβ-ezrin pathway during confined migration.

PIEZO1 activity is required for neuronal migration in confined brain tissue

We further examined the functional significance of PIEZO1 in CGN migration in a confined microenvironment. The migratory capacity of CGNs from wild-type and PIEZO1 cKO mice was analyzed using a reaggregate culture[32] either inside (3D) or on the surface (2D) of Matrigel. There was no apparent difference in migratory capacity between wild-type and PIEZO1 cKO neurons in the 2D culture on the Matrigel surface, whereas PIEZO1 cKO neurons exhibited a significant delay in 3D migration within Matrigel (Figures 5A and 5B).

We next transfected MRLC-2GFP in dissociated CGNs from wild-type and PIEZO1 cKO mice and subjected them to 2D and 3D Matrigel cultures. Myosin was enriched in the front cytoplasm in cells migrating in the 2D environment in both wild-type and PIEZO1 cKO cells. In the 3D matrix, myosin was localized at the periphery of the posterior part of the soma in wild-type cells. On the other hand, in PIEZO1-deficient cells, myosin failed to translocate to the posterior membrane and resides in the leading process, much like in 2D culture (Figures 5C–5E; Video S11). We next performed the same experiments using ezrin-GFP. In wild-type cells, ezrin showed no pronounced localization in the 2D

(F) Translocation of ezrin (top) and actin (bottom) to the plasma membrane after Yoda1 treatment. (F′ and F″) Cortical enrichment of ezrin (F′) and actin (F″) along the circumference of the cell soma upon treatment with Yoda1. Relative intensity of the signal in the cell cortex to the signal in the adjacent cytoplasm is shown.
(G) Translocation of ezrin to the plasma membrane before and 120 s after treatments with DMSO, Yoda1, Yoda1 and BAPTA, or Yoda1 and LY333531. The cell soma is subdivided into 4 anteroposterior parts. $^*p < 0.05$ (middle front, middle rear, and rear; before and after drug treatment) and $^{**}p < 0.01$ (front), Wilcoxon test. $n \geq 6$ neurons per condition.
(H) Colocalization of ezrin and actomyosin before and 120 s after drug treatments.
Samples were collected from more than three independent experiments. $^*p < 0.05$, Wilcoxon test. $n \geq 6$ neurons per condition. Data are represented as mean ± SEM. Scale bars, 2 μm (A and F) and 5 μm (E). See also Figure S4 and Videos S8, S9, and S10.

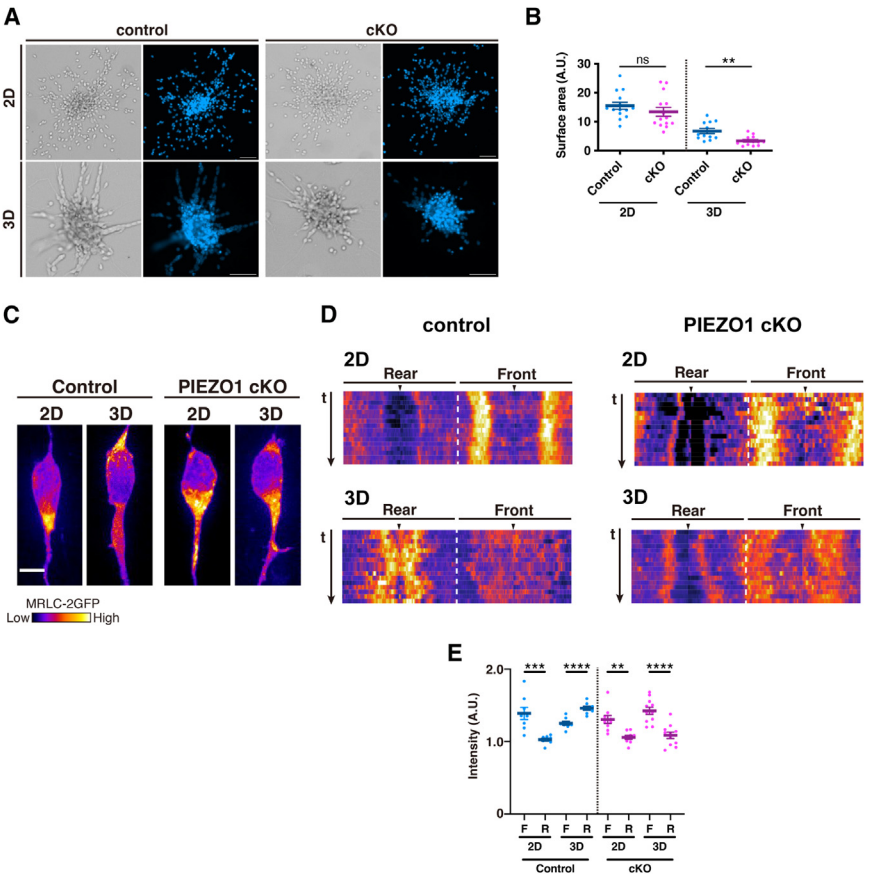

Figure 5. PIEZO1 signaling is required for myosin translocation and CGN migration in confined microenvironments

(A) Migration of CGNs from wild-type (control) and PIEZO1 cKO mice in reaggregate cultures. Reaggregates were plated on the surface (2D) or embedded in Matrigel (3D).

(B) Migration distance of CGNs from the reaggregate periphery in each condition. $^{**}p < 0.01$, Mann-Whitney test. $n = 14$ reaggregates per condition.

(C) Snapshot images of wild-type and PIEZO1 cKO CGNs transfected with MRLC-2GFP in 2D and 3D reaggregate cultures.

(D) Temporal dynamics of cortical MRLC-2GFP signals along the circumference of the cell soma.

(E) The rear/front distribution of cortical MRLC-2GFP signals in migrating CGNs from wild-type mice and PIEZO1 cKO in 2D and 3D Matrigel culture. The signal intensity was averaged over 10 frames per minute for a 10-min observation. $^{**}p < 0.01$, $^{***}p < 0.001$, and $^{****}p < 0.0001$, unpaired t test. $n \geq 8$ neurons per condition.

Samples were collected from more than three independent experiments. Scale bars, 50 μm (A) and 5 μm (C). Data are represented as mean ± SEM. See also Figure S5 and Videos S11 and S12.

environment, while it clearly localized at the posterior membrane in 3D culture. Such differential localization was not seen in PIEZO1-deficient cells, but ezrin distributed in the entire cell soma in both 2D and 3D conditions (Figure S5; Video S12). These results support the notion that PIEZO1 is activated in confined spaces and induces ezrin and myosin translocation to the plasma membrane at the cell rear.

We then asked whether PIEZO1 function is involved in CGN migration *in vivo*. CGNs are born in the EGL and undergo radial migration toward the IGL during the first to third postnatal weeks. In contrast to the severe migration defects in PIEZO1 cKO cells in 3D culture, there was no apparent difference in the gross morphology of the cerebellar cortices in wild-type and PIEZO1 cKO mice (Figures 6A and 6B). For more accurate analysis, we administrated BrdU to label granule cell progenitors at postnatal day (P)9 and tracked BrdU-positive CGNs in P13 cerebelli from wild-type and PIEZO1 cKO mice. There was no difference in the number of BrdU-positive cells in wild-type and PIEZO1 cKO mice (Figure 6C). However, we found a slight but significant increase in the number of CGNs that had stopped at the Purkinje cell layer (PCL) in PIEZO1 cKO mice. In contrast, fewer CGNs reached the lower IGL in PIEZO1 cKO mice, suggesting that CGN migration is delayed in crowded tissue space in the absence of PIEZO1 (Figures 6D and 6E). These results indicate that PIEZO1 activity is required for the migration of CGNs in the developing cerebellum.

DISCUSSION

We have demonstrated that neurons switch their migration modes by sensing the extracellular microenvironment in the developing brain. Migration is driven by the adhesion-based traction generated in the cell front in a non-confined environment, but when CGNs encounter a constricted space, they exert an actomyosin contractile force at the cell rear to squeeze into the constriction. The multi-step processes of confined migration of neurons depicted by the present study include (1) the entry of the cell front into a constriction and expected increase in internal pressure and membrane tension in the cell soma, (2) PIEZO1 activation and Ca^{2+} influx, (3) activation of Ca^{2+}-dependent PKC, (4) ezrin-actomyosin coupling to the posterior plasma membrane, and (5) forward propulsion by the actomyosin contractile force at the rear (Figure S6).

It remains unanswered as to why the actomyosin concentration is biased toward the rear, as the internal pressure should increase uniformly upon entry into the confined space. It has recently been demonstrated that PIEZO1 is not uniformly distributed in the plasma membrane but is excluded from fine protrusions with high membrane curvature, raising the possibility that subcellular localization of PIEZO1 is biased in migrating neurons.[53] However, we observed that PIEZO1 protein was distributed throughout the soma and processes in both 2D and 3D conditions (Figure 4). Furthermore, Yoda1 treatment in non-confined culture dishes induced Ca^{2+} influx throughout the cell soma and leading process (Video S6). Thus, it is likely that PIEZO1 is constitutively expressed in migrating CGNs and perceptible for mechanical stimuli over a large cell surface area. Notably,

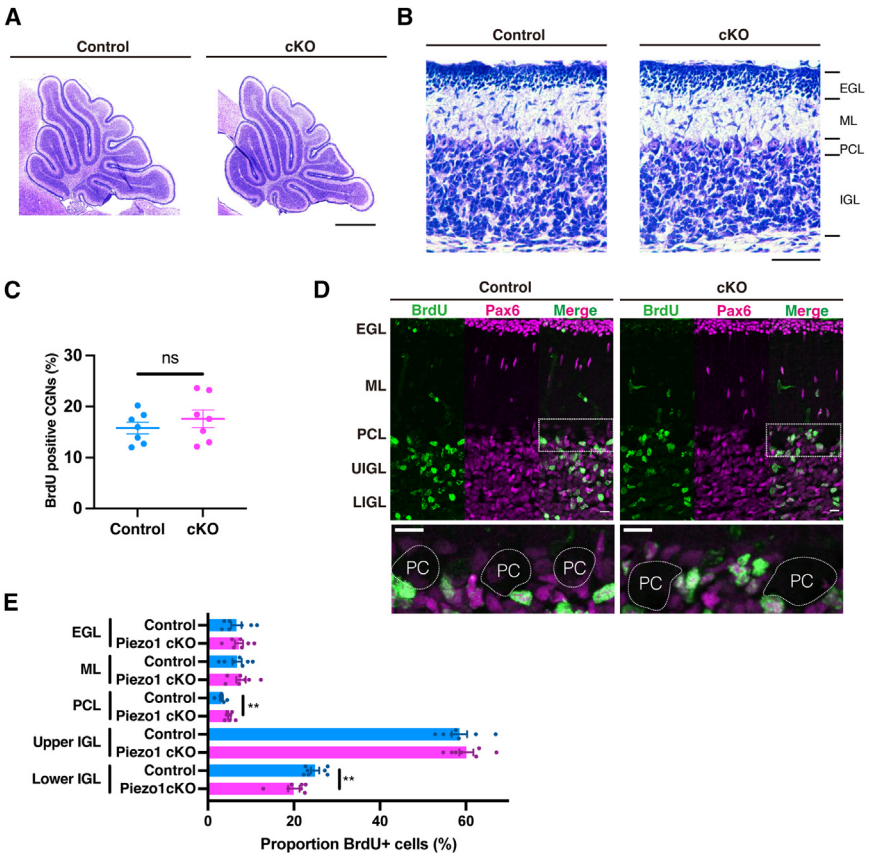

Figure 6. Delayed migration of CGNs in PIEZO1 cKO mice

(A) Sagittal cerebellar sections of control (Piezo1$^{flox/flox}$) and PIEZO1 cKO (NeuroD1-Cre; Piezo1$^{flox/flox}$) mice at P9 were stained with cresyl violet (Nissl staining).

(B) Magnified views of the cerebellar cortices.

(C) The number of CGNs labeled with BrdU in wild-type and PIEZO1 cKO mice. $n \geq 1{,}700$ neurons per condition.

(D) BrdU (green) and Pax6 (magenta) labeling of P13 cerebella after BrdU injection at P9. Magnified views of the PC layer are shown along the bottom.

(E) Proportion of BrdU+ CGNs in each layer. Data were collected from 7 mice of respective genotypes in 4 independent experiments. $^{**}p < 0.01$, Mann-Whitney test. $n \geq 400$ neurons per condition.

Data are represented as mean ± SEM. Scale bars, 500 μm (A), 50 μm (B), and 10 μm (D).

however, ezrin translocation was strongly biased to the posterior membrane by bath-applied Yoda1 in non-confined spaces, suggesting that downstream signals are preferentially activated posteriorly in migrating CGNs. Asymmetric shape and/or molecular distribution in the polarized neuron may contribute to the local activation of ezrin and actomyosin at the cell rear.[5]

We observe that cortical interneurons also switch between multiple migration modes. A recent study using retinal neurons has demonstrated a similar mode switch and posterior enrichment of actomyosin during confined migration in crowded tissue,[54] yet whether they use the same signaling pathway as CGNs is unknown.

PIEZO1 has been identified as a switch, altering migration modes in confined space in multiple cell systems.[55–57] Piezo1-induced Ca^{2+} influx and actin remodeling are commonly involved in all cases, although the signaling mechanisms are diverse. In cultured CHO cells, PIEZO1 induces cell stiffening during confined migration by inhibiting PKA through the Ca^{2+}/phosphodiesterase 1 axis.[56] Besides PIEZO1, other MSCs have been implicated in confined migration in various cell types. For instance, TRPV4 is overexpressed in highly invasive breast cancer cells and has been shown to induce the phosphorylation of ERM proteins.[58] TRPV4 activity has also been implicated in elevating osmotic pressure in the cell front, propelling forward the migration of mesenchymal stem cells in a confined space.[59] In contrast, inhibition of TRPV4 by HC-067047 suppressed both confined and non-confined migration in our CGNs (Figure 3). Thus, strategies for 3D migration might be more diverse among various cell types than currently understood.

Switching between motility modes in 2D and 3D environments is also observed in axonal growth cones. In mouse hippocampal neurons situated in a 3D environment, growth cone extension does not require the traction force generated by the cell-substrate adhesion, in contrast to the adhesion-dependent mechanism in 2D environment.[60] Although the causality is unknown, PIEZO1 and other MSCs have been implicated in growth cone navigation in the developing brain.[41,61] In frog spinal axons, TRPC1 regulates growth cone extension through the activation of calpain-mediated proteolysis of adhesion molecules.[61,62] A previous report using rat hippocampal neurons has demonstrated that calpain also mediates degradation of drebrin, a key regulator of traction force in the leading process during CGN migration in the 2D environment,[27,63] As PIEZO1-induced Ca^{2+} has been shown to activate calpain,[64] the activation of PIEZO1 in 3D confinement may not only promote actomyosin contraction in the cell rear via the PKC-ezrin pathway but may also induce calpain-dependent adhesion breakdown in the leading process. New experimental systems, such as traction force microscopy and total internal reflection fluorescence microscopy (TIRFM) in microfluidic devices, would help to clarify the mechanisms of mode change in various subcellular compartments and how they integrally drive whole-cell movement.[65]

Limitations of the study

While our work demonstrates the role of PIEZO1 in 3D confined migration and its downstream molecular signaling, the actual subcellular force distribution in 2D and 3D migration in the presence or absence of PIEZO1 is unknown. 3D traction force microscopy may help to clarify the dynamic force generation during neuronal migration in various environments. In addition, the

mechanical properties of the brain tissue, such as tissue stiffness and the size of the interstitial spaces, have not been assessed. PIEZO1 function in cell migration in other brain regions also remains to be clarified.

RESOURCE AVAILABILITY

Lead contact

Further information and requests for resources and reagents should be directed to and will be fulfilled by the lead contact, Naotaka Nakazawa (nakazawa.naotaka@emat.kindai.ac.jp).

Materials availability

Plasmids generated in this study will be made available upon request or will be deposited to Addgene in the future. This study did not generate new unique reagents.

Data and code availability

- RNA-seq data are available at DDBJ (https://www.ddbj.nig.ac.jp/index-e.html). Accession numbers are listed in the key resources table and are publicly available as of the date of publication.
- The original Python code to create the heatmaps of the image data is available from the lead contact upon request.
- Any additional information required to reanalyze the data reported in this paper is available from the lead contact upon request.

ACKNOWLEDGMENTS

We thank F. Margadant, H. Xian, H. Umeshima, and M. Nishiyama for invaluable discussions; G. Zimmer-Bensch, D. Pensold, M. Sawada, and K. Sawamoto for culture protocols; iCeMS Analysis Center at Kyoto University for technical assistance with imaging using a Dragonfly microscope; and A. Patapoutian for the kind gift of the Piezo$^{flox/flox}$ mouse line. This work was supported by grants from Japan Society for the Promotion of Science (JSPS) Kakenhi 18KK0212 (M.K., N.N., and G.G.), 20H00483, 16H06484, and 22H05169 (M.K.), 21H05126 (N.N.), 16H06486 (T.A.), and 20H03387 and 21H05125 (K.N.); AMED 23gm1910002 (M.K.) and 20gm6310014 (K.N.); The Naito Foundation (K.N.); the Mitsubishi Foundation (K.N.); the Takeda Science Foundation (N.N.); the Mochida Memorial Foundation (N.N.); and JST FOREST Program JPMJFR225J (N.N.) and JPMJFR22D (Y.K.).

AUTHOR CONTRIBUTIONS

N.N. and M.K. conceived the project and designed the experiments. G.G. designed and generated micropatterned substrates. N.N., J.K., N.T., K.T., and K.N. performed the experiments. Y.K., T.S., and T.A. performed the modeling. M.K. and N.N. wrote the manuscript with input from all authors.

DECLARATION OF INTERESTS

The authors declare that they have no competing interests.

STAR★METHODS

Detailed methods are provided in the online version of this paper and include the following:

SUPPLEMENTAL INFORMATION

Supplemental information can be found online at https://doi.org/10.1016/j.celrep.2025.115405.

Received: May 11, 2024
Revised: January 9, 2025
Accepted: February 14, 2025

REFERENCES

1. Ridley, A.J., Schwartz, M.A., Burridge, K., Firtel, R.A., Ginsberg, M.H., Borisy, G., Parsons, J.T., and Horwitz, A.R. (2003). Cell migration: integrating signals from front to back. Science *302*, 1704–1709.
2. Case, L.B., and Waterman, C.M. (2015). Integration of actin dynamics and cell adhesion by a three-dimensional, mechanosensitive molecular clutch. Nat. Cell Biol. *17*, 955–963.
3. Krause, M., and Gautreau, A. (2014). Steering cell migration: lamellipodium dynamics and the regulation of directional persistence. Nat. Rev. Mol. Cell Biol. *15*, 577–590.
4. Yamada, K.M., and Sixt, M. (2019). Mechanisms of 3D cell migration. Nat. Rev. Mol. Cell Biol. *20*, 738–752.
5. Callan-Jones, A.C., and Voituriez, R. (2016). Actin flows in cell migration: from locomotion and polarity to trajectories. Curr. Opin. Cell Biol. *38*, 12–17.
6. Marks, P.C., and Petrie, R.J. (2022). Push or pull: how cytoskeletal crosstalk facilitates nuclear movement through 3D environments. Phys. Biol. *19*, 021003. https://doi.org/10.1088/1478-3975/ac45e3.
7. Bergert, M., Chandradoss, S.D., Desai, R.A., and Paluch, E. (2012). Cell mechanics control rapid transitions between blebs and lamellipodia during migration. Proc. Natl. Acad. Sci. USA *109*, 14434–14439.
8. Wolf, K., Te Lindert, M., Krause, M., Alexander, S., Te Riet, J., Willis, A.L., Hoffman, R.M., Figdor, C.G., Weiss, S.J., and Friedl, P. (2013). Physical limits of cell migration: control by ECM space and nuclear deformation and tuning by proteolysis and traction force. J. Cell Biol. *201*, 1069–1084.
9. Fraley, S.I., Feng, Y., Krishnamurthy, R., Kim, D.-H., Celedon, A., Longmore, G.D., and Wirtz, D. (2010). A distinctive role for focal adhesion proteins in three-dimensional cell motility. Nat. Cell Biol. *12*, 598–604.
10. Stroka, K.M., Jiang, H., Chen, S.-H., Tong, Z., Wirtz, D., Sun, S.X., and Konstantopoulos, K. (2014). Water permeation drives tumor cell migration in confined microenvironments. Cell *157*, 611–623.
11. Ruprecht, V., Wieser, S., Callan-Jones, A., Smutny, M., Morita, H., Sako, K., Barone, V., Ritsch-Marte, M., Sixt, M., Voituriez, R., and Heisenberg, C.P. (2015). Cortical contractility triggers a stochastic switch to fast amoeboid cell motility. Cell *160*, 673–685.
12. Blaser, H., Reichman-Fried, M., Castanon, I., Dumstrei, K., Marlow, F.L., Kawakami, K., Solnica-Krezel, L., Heisenberg, C.-P., and Raz, E. (2006). Migration of zebrafish primordial germ cells: a role for myosin contraction and cytoplasmic flow. Dev. Cell *11*, 613–627.
13. Liu, Y.-J., Le Berre, M., Lautenschlaeger, F., Maiuri, P., Callan-Jones, A., Heuzé, M., Takaki, T., Voituriez, R., and Piel, M. (2015). Confinement and

low adhesion induce fast amoeboid migration of slow mesenchymal cells. Cell *160*, 659–672.

14. Hung, W.-C., Chen, S.-H., Paul, C.D., Stroka, K.M., Lo, Y.-C., Yang, J.T., and Konstantopoulos, K. (2013). Distinct signaling mechanisms regulate migration in unconfined versus confined spaces. J. Cell Biol. *202*, 807–824.
15. Lämmermann, T., Bader, B.L., Monkley, S.J., Worbs, T., Wedlich-Söldner, R., Hirsch, K., Keller, M., Förster, R., Critchley, D.R., Fässler, R., and Sixt, M. (2008). Rapid leukocyte migration by integrin-independent flowing and squeezing. Nature *453*, 51–55.
16. Thiam, H.-R., Vargas, P., Carpi, N., Crespo, C.L., Raab, M., Terriac, E., King, M.C., Jacobelli, J., Alberts, A.S., Stradal, T., et al. (2016). Perinuclear Arp2/3-driven actin polymerization enables nuclear deformation to facilitate cell migration through complex environments. Nat. Commun. *7*, 10997.
17. Wilson, K., Lewalle, A., Fritzsche, M., Thorogate, R., Duke, T., and Charras, G. (2013). Mechanisms of leading edge protrusion in interstitial migration. Nat. Commun. *4*, 2896.
18. Minegishi, T., and Inagaki, N. (2020). Forces to Drive Neuronal Migration Steps. Front. Cell Dev. Biol. *8*, 863.
19. Nakazawa, N., and Kengaku, M. (2020). Mechanical Regulation of Nuclear Translocation in Migratory Neurons. Front. Cell Dev. Biol. *8*, 150.
20. Schaar, B.T., and McConnell, S.K. (2005). Cytoskeletal coordination during neuronal migration. Proc. Natl. Acad. Sci. USA *102*, 13652–13657.
21. Bellion, A., Baudoin, J.-P., Alvarez, C., Bornens, M., and Métin, C. (2005). Nucleokinesis in tangentially migrating neurons comprises two alternating phases: forward migration of the Golgi/centrosome associated with centrosome splitting and myosin contraction at the rear. J. Neurosci. *25*, 5691–5699.
22. Martini, F.J., and Valdeolmillos, M. (2010). Actomyosin contraction at the cell rear drives nuclear translocation in migrating cortical interneurons. J. Neurosci. *30*, 8660–8670.
23. Shinohara, R., Thumkeo, D., Kamijo, H., Kaneko, N., Sawamoto, K., Watanabe, K., Takebayashi, H., Kiyonari, H., Ishizaki, T., Furuyashiki, T., and Narumiya, S. (2012). A role for mDia, a Rho-regulated actin nucleator, in tangential migration of interneuron precursors. Nat. Neurosci. *15*, 373–380.
24. Silva, C.G., Peyre, E., Adhikari, M.H., Tielens, S., Tanco, S., Van Damme, P., Magno, L., Krusy, N., Agirman, G., Magiera, M.M., et al. (2018). Cell-Intrinsic Control of Interneuron Migration Drives Cortical Morphogenesis. Cell *172*, 1063–1078.e19.
25. Jiang, J., Zhang, Z.-H., Yuan, X.-B., and Poo, M.-M. (2015). Spatiotemporal dynamics of traction forces show three contraction centers in migratory neurons. J. Cell Biol. *209*, 759–774.
26. Solecki, D.J., Trivedi, N., Govek, E.-E., Kerekes, R.A., Gleason, S.S., and Hatten, M.E. (2009). Myosin II motors and F-actin dynamics drive the coordinated movement of the centrosome and soma during CNS glial-guided neuronal migration. Neuron *63*, 63–80.
27. Trivedi, N., Stabley, D.R., Cain, B., Howell, D., Laumonnerie, C., Ramahi, J.S., Temirov, J., Kerekes, R.A., Gordon-Weeks, P.R., and Solecki, D.J. (2017). Drebrin-mediated microtubule-actomyosin coupling steers cerebellar granule neuron nucleokinesis and migration pathway selection. Nat. Commun. *8*, 14484.
28. Umeshima, H., Nomura, K.-I., Yoshikawa, S., Hörning, M., Tanaka, M., Sakuma, S., Arai, F., Kaneko, M., and Kengaku, M. (2019). Local traction force in the proximal leading process triggers nuclear translocation during neuronal migration. Neurosci. Res. *142*, 38–48.
29. Trivedi, N., and Solecki, D.J. (2011). Neuronal migration illuminated: a look under the hood of the living neuron. Cell Adhes. Migrat. *5*, 42–47.
30. Kengaku, M. (2018). Cytoskeletal control of nuclear migration in neurons and non-neuronal cells. Proc. Jpn. Acad. Ser. B Phys. Biol. Sci. *94*, 337–349.
31. Wu, Y.K., Umeshima, H., Kurisu, J., and Kengaku, M. (2018). Nesprins and opposing microtubule motors generate a point force that drives directional nuclear motion in migrating neurons. Development *145*, dev158782. https://doi.org/10.1242/dev.158782.
32. Umeshima, H., Hirano, T., and Kengaku, M. (2007). Microtubule-based nuclear movement occurs independently of centrosome positioning in migrating neurons. Proc. Natl. Acad. Sci. USA *104*, 16182–16187.
33. Poincloux, R., Collin, O., Lizárraga, F., Romao, M., Debray, M., Piel, M., and Chavrier, P. (2011). Contractility of the cell rear drives invasion of breast tumor cells in 3D Matrigel. Proc. Natl. Acad. Sci. USA *108*, 1943–1948.
34. Harada, T., Swift, J., Irianto, J., Shin, J.-W., Spinler, K.R., Athirasala, A., Diegmiller, R., Dingal, P.C.D.P., Ivanovska, I.L., and Discher, D.E. (2014). Nuclear lamin stiffness is a barrier to 3D migration, but softness can limit survival. J. Cell Biol. *204*, 669–682.
35. Lee, S.-Y., and MacKinnon, R. (2004). A membrane-access mechanism of ion channel inhibition by voltage sensor toxins from spider venom. Nature *430*, 232–235.
36. Suchyna, T.M., Johnson, J.H., Hamer, K., Leykam, J.F., Gage, D.A., Clemo, H.F., Baumgarten, C.M., and Sachs, F. (2000). Identification of a peptide toxin from Grammostola spatulata spider venom that blocks cation-selective stretch-activated channels. J. Gen. Physiol. *115*, 583–598.
37. Miyamoto, T., Mochizuki, T., Nakagomi, H., Kira, S., Watanabe, M., Takayama, Y., Suzuki, Y., Koizumi, S., Takeda, M., and Tominaga, M. (2014). Functional role for Piezo1 in stretch-evoked Ca^{2+} influx and ATP release in urothelial cell cultures. J. Biol. Chem. *289*, 16565–16575.
38. Merritt, J.E., Armstrong, W.P., Benham, C.D., Hallam, T.J., Jacob, R., Jaxa-Chamiec, A., Leigh, B.K., McCarthy, S.A., Moores, K.E., and Rink, T.J. (1990). SK&F 96365, a novel inhibitor of receptor-mediated calcium entry. Biochem. J. *271*, 515–522.
39. Everaerts, W., Zhen, X., Ghosh, D., Vriens, J., Gevaert, T., Gilbert, J.P., Hayward, N.J., McNamara, C.R., Xue, F., Moran, M.M., et al. (2010). Inhibition of the cation channel TRPV4 improves bladder function in mice and rats with cyclophosphamide-induced cystitis. Proc. Natl. Acad. Sci. USA *107*, 19084–19089.
40. Cahalan, S.M., Lukacs, V., Ranade, S.S., Chien, S., Bandell, M., and Patapoutian, A. (2015). Piezo1 links mechanical forces to red blood cell volume. Elife *4*, e07370. https://doi.org/10.7554/eLife.07370.
41. Koser, D.E., Thompson, A.J., Foster, S.K., Dwivedy, A., Pillai, E.K., Sheridan, G.K., Svoboda, H., Viana, M., Costa, L.d.F., Guck, J., et al. (2016). Mechanosensing is critical for axon growth in the developing brain. Nat. Neurosci. *19*, 1592–1598.
42. Ranade, S.S., Qiu, Z., Woo, S.-H., Hur, S.S., Murthy, S.E., Cahalan, S.M., Xu, J., Mathur, J., Bandell, M., Coste, B., et al. (2014). Piezo1, a mechanically activated ion channel, is required for vascular development in mice. Proc. Natl. Acad. Sci. USA *111*, 10347–10352.
43. Syeda, R., Xu, J., Dubin, A.E., Coste, B., Mathur, J., Huynh, T., Matzen, J., Lao, J., Tully, D.C., Engels, I.H., et al. (2015). Chemical activation of the mechanotransduction channel Piezo1. Elife *4*, e07369. https://doi.org/10.7554/eLife.07369.
44. Chen, T.-W., Wardill, T.J., Sun, Y., Pulver, S.R., Renninger, S.L., Baohan, A., Schreiter, E.R., Kerr, R.A., Orger, M.B., Jayaraman, V., et al. (2013). Ultrasensitive fluorescent proteins for imaging neuronal activity. Nature *499*, 295–300.
45. Coste, B., Mathur, J., Schmidt, M., Earley, T.J., Ranade, S., Petrus, M.J., Dubin, A.E., and Patapoutian, A. (2010). Piezo1 and Piezo2 are essential components of distinct mechanically activated cation channels. Science *330*, 55–60.
46. Gudipaty, S.A., Lindblom, J., Loftus, P.D., Redd, M.J., Edes, K., Davey, C.F., Krishnegowda, V., and Rosenblatt, J. (2017). Mechanical stretch triggers rapid epithelial cell division through Piezo1. Nature *543*, 118–121.

47. Komuro, H., and Rakic, P. (1996). Intracellular Ca2+ fluctuations modulate the rate of neuronal migration. Neuron *17*, 275–285.

48. Ng, T., Parsons, M., Hughes, W.E., Monypenny, J., Zicha, D., Gautreau, A., Arpin, M., Gschmeissner, S., Verveer, P.J., Bastiaens, P.I., and Parker, P.J. (2001). Ezrin is a downstream effector of trafficking PKC–integrin complexes involved in the control of cell motility. EMBO J. *20*, 2723–2741.

49. Clucas, J., and Valderrama, F. (2015). ERM proteins in cancer progression. J. Cell Sci. *128*, 1253.

50. Endo, K., Kondo, S., Shackleford, J., Horikawa, T., Kitagawa, N., Yoshizaki, T., Furukawa, M., Zen, Y., and Pagano, J.S. (2009). Phosphorylated ezrin is associated with EBV latent membrane protein 1 in nasopharyngeal carcinoma and induces cell migration. Oncogene *28*, 1725–1735.

51. Turunen, O., Wahlström, T., and Vaheri, A. (1994). Ezrin has a COOH-terminal actin-binding site that is conserved in the ezrin protein family. J. Cell Biol. *126*, 1445–1453.

52. Fehon, R.G., McClatchey, A.I., and Bretscher, A. (2010). Organizing the cell cortex: the role of ERM proteins. Nat. Rev. Mol. Cell Biol. *11*, 276–287.

53. Yang, S., Miao, X., Arnold, S., Li, B., Ly, A.T., Wang, H., Wang, M., Guo, X., Pathak, M.M., Zhao, W., et al. (2022). Membrane curvature governs the distribution of Piezo1 in live cells. Nat. Commun. *13*, 7467.

54. Amini, R., Bhatnagar, A., Schlüßler, R., Möllmert, S., Guck, J., and Norden, C. (2022). Amoeboid-like migration ensures correct horizontal cell layer formation in the developing vertebrate retina. Elife *11*, e76408. https://doi.org/10.7554/eLife.76408.

55. Canales Coutiño, B., and Mayor, R. (2021). The mechanosensitive channel Piezo1 cooperates with semaphorins to control neural crest migration. Development *148*, dev200001. https://doi.org/10.1242/dev.200001.

56. Hung, W.-C., Yang, J.R., Yankaskas, C.L., Wong, B.S., Wu, P.-H., Pardo-Pastor, C., Serra, S.A., Chiang, M.-J., Gu, Z., Wirtz, D., et al. (2016). Confinement Sensing and Signal Optimization via Piezo1/PKA and Myosin II Pathways. Cell Rep. *15*, 1430–1441.

57. Srivastava, N., Traynor, D., Piel, M., Kabla, A.J., and Kay, R.R. (2020). Pressure sensing through Piezo channels controls whether cells migrate with blebs or pseudopods. Proc. Natl. Acad. Sci. USA *117*, 2506–2512.

58. Lee, W.H., Choong, L.Y., Mon, N.N., Lu, S., Lin, Q., Pang, B., Yan, B., Krishna, V.S.R., Singh, H., Tan, T.Z., et al. (2016). TRPV4 Regulates Breast Cancer Cell Extravasation, Stiffness and Actin Cortex. Sci. Rep. *6*, 27903.

59. Lee, H.-P., Alisafaei, F., Adebawale, K., Chang, J., Shenoy, V.B., and Chaudhuri, O. (2021). The nuclear piston activates mechanosensitive ion channels to generate cell migration paths in confining microenvironments. Sci. Adv. *7*, eabd4058. https://doi.org/10.1126/sciadv.abd4058.

60. Santos, T.E., Schaffran, B., Broguière, N., Meyn, L., Zenobi-Wong, M., and Bradke, F. (2020). Axon Growth of CNS Neurons in Three Dimensions Is Amoeboid and Independent of Adhesions. Cell Rep. *32*, 107907.

61. Kerstein, P.C., Jacques-Fricke, B.T., Rengifo, J., Mogen, B.J., Williams, J.C., Gottlieb, P.A., Sachs, F., and Gomez, T.M. (2013). Mechanosensitive TRPC1 channels promote calpain proteolysis of talin to regulate spinal axon outgrowth. J. Neurosci. *33*, 273–285.

62. Kerstein, P.C., Patel, K.M., and Gomez, T.M. (2017). Calpain-Mediated Proteolysis of Talin and FAK Regulates Adhesion Dynamics Necessary for Axon Guidance. J. Neurosci. *37*, 1568–1580.

63. Chimura, T., Launey, T., and Yoshida, N. (2015). Calpain-Mediated Degradation of Drebrin by Excitotoxicity In vitro and In vivo. PLoS One *10*, e0125119.

64. Liu, T.-T., Du, X.-F., Zhang, B.-B., Zi, H.-X., Yan, Y., Yin, J.-A., Hou, H., Gu, S.-Y., Chen, Q., and Du, J.-L. (2020). Piezo1-Mediated Ca2+ Activities Regulate Brain Vascular Pathfinding during Development. Neuron *108*, 180–192.e5.

65. Yip, A.K., Chiam, K.-H., and Matsudaira, P. (2015). Traction stress analysis and modeling reveal that amoeboid migration in confined spaces is accompanied by expansive forces and requires the structural integrity of the membrane-cortex interactions. Integr. Biol. *7*, 1196–1211.

66. Sawada, M., Matsumoto, M., Narita, K., Kumamoto, N., Ugawa, S., Takeda, S., and Sawamoto, K. (2020). In vitro Time-lapse Imaging of Primary Cilium in Migrating Neuroblasts. Bio. Protoc. *10*, e3823.

67. Nakazawa, N., Sathe, A.R., Shivashankar, G.V., and Sheetz, M.P. (2016). Matrix mechanics controls FHL2 movement to the nucleus to activate p21 expression. Proc. Natl. Acad. Sci. USA *113*, E6813–E6822.

68. Kameo, Y., Ozasa, M., and Adachi, T. (2022). Computational framework for analyzing flow-induced strain on osteocyte as modulated by microenvironment. J. Mech. Behav. Biomed. Mater. *126*, 105027.

69. Yokoyama, Y., Kameo, Y., Kamioka, H., and Adachi, T. (2021). High-resolution image-based simulation reveals membrane strain concentration on osteocyte processes caused by tethering elements. Biomech. Model. Mechanobiol. *20*, 2353–2360.

70. Skalak, R., Tozeren, A., Zarda, R.P., and Chien, S. (1973). Strain energy function of red blood cell membranes. Biophys. J. *13*, 245–264.

71. Li, J., Dao, M., Lim, C.T., and Suresh, S. (2005). Spectrin-level modeling of the cytoskeleton and optical tweezers stretching of the erythrocyte. Biophys. J. *88*, 3707–3719.

72. Chen, S., and Doolen, G.D. (1998). Lattice Boltzmann method for fluid flows. Annu. Rev. Fluid Mech. *30*, 329–364.

73. Peskin, C.S. (2002). The immersed boundary method. Acta Numer. *11*, 479–517.

74. Puig-de-Morales-Marinkovic, M., Turner, K.T., Butler, J.P., Fredberg, J.J., and Suresh, S. (2007). Viscoelasticity of the human red blood cell. Am. J. Physiol. Cell Physiol. *293*, C597–C605.

75. Spedden, E., White, J.D., Naumova, E.N., Kaplan, D.L., and Staii, C. (2012). Elasticity maps of living neurons measured by combined fluorescence and atomic force microscopy. Biophys. J. *103*, 868–877.

STAR★METHODS

KEY RESOURCES TABLE

REAGENT or RESOURCE	SOURCE	IDENTIFIER
Antibodies		
Mouse anti-Ezrin monoclonal antibody	Abcam	Cat#ab4069; RRID:AB_304261
Rabbit anti-Ezrin (phospho T567) polyclonal antibody	Abcam	Cat# ab47293; RRID:AB_873790
Mouse anti-GAPDH monoclonal antibody	Abcam	Cat# ab8245; RRID:AB_2107448
Rabbit anti-Pax6 polyclonal antibody	FUJIFILM Wako Pure Chemical Corporation	Cat# 015–27293; RRID:AB_3094969
Mouse anti-BrdU monoclonal antibody	Sigma-Aldrich	Cat# B2531; RRID:AB_476793
Living colors dsRed Polyclonal antibody(Anti-DsRed)	Takara Bio	Cat# 632496; RRID:AB_10013483
HRP-conjugated anti-rabbit antibody	Bio-Rad	Cat# 172–1019; RRID:AB_11125143
HRP-conjugated anti-mouse antibody	Bio-Rad	Cat# 1706516; RRID:AB_2921252
Bacterial and virus strains		
DynaCompetent Cells Jet DH5α	BDL	DS225
One Shot™ *ccd*B Survival™ 2 T1^R Competent Cells	ThermoFisher	A10460
Chemicals, peptides, and recombinant proteins		
blebbistatin	Sigma	B0560
cytochalasin D	TOCRIS	1233
latrunculin B	KOM	AG-CN2-0031-M001
jasplakinolide	CALBIOCHEM	420107
GsMTx4	Abcam	ab141871
SKF96365	CALBIOCHEM	567310
HC-067047	Millipore	616521
Yoda1	Sigma	SML1558
Dooku1	TOCRIS	6568
BAPTA, extracellular calcium chelator	Abcam	ab144924
EGTA	ThermoFisher	E1219
thapsigargin	Abcam	ab120286
Gö6983	CALBIOCHEM	365251
LY333531	Enzo	ALX-270-348
NSC668394	Millipore	341216
NSC23766	CALBIOCHEM	553502
Rho inhibitor I	Cytoskeleton	CT04
ML141	TOCRIS	4266
Agarose	Nacalai tesque	01161–12
Cellmatrix	Nitta Gelatin	Type I-A
HBSS	Gibco	14170–112
BME	Sigma	B9638-1L
Earle's balanced salt	Sigma	E6132
horse serum	Gibco	26050–070
sodium pyruvate	Sigma	S8636-100ML
D-glucose	Sigma	G7021-100G
sodium bicarbonate	Sigma	S5761-500G
N-2 supplement	Gibco	17502–001
Matrigel (Growth Factor Reduced)	Corning	354230

(*Continued on next page*)

Continued

REAGENT or RESOURCE	SOURCE	IDENTIFIER
bovine serum albumin	Sigma Aldrich	A3156-5G
Penicillin-Streptomycin	Gibco	15140–122
Trypsin	Nacalai tesque	18172–94
poly-*d*-lysine	Sigma Aldrich	P6407
Laminin	Sigma Aldrich	L2020-1MG
Protease inhibitor cocktail (EDTA free)	Nacalai tesque	03969–21
Phosphatase inhibitor cocktail	Sigma	
Tween 20	Nacalai tesque	28353–85
skimmed powder milk	BD	232100
5-bromo-2′-deoxyuridine (BrdU)	Invitrogen(sigma)	B5002-1G
isoflurane	Mairan Pharma	
paraformaldehyde (PFA)	Nacalai tesque	02890–45
DAPI	Nacalai tesque	11034–56
Fluoromount	DBS(Diagnostic BioSystems)	K024
Cresyl violet	MP Biomedicals	150727
Critical commercial assays		
KOD FX polymerase kit	Toyobo	KFX-101
Neuron Dissociation Kit	Wako Pure Chemical Industries, Ltd	291–78001
lipofectamine 2000	Thermo Fisher Scientific	11668–019
Protein assay BCA kit	Nacalai tesque	06385–00
ECL Prime	G.E. Healthcare	RPN2232
RNAeasy Mini Kit	QIAGEN	74104
Gateway LR Clonase II Enzyme Mix	Invitrogen	11791
Deposited data		
Primary sequencing data deposited	DDBJ	DDBJ : PRJDB20245
Experimental models: Organisms/strains		
Mouse: Slc:ICR	Japan SLC	RRID:MGI:5462094
Mouse: C57BL/6	Japan SLC	RRID:MGI:5488963
Mouse: *PIEZO1*$^{flox/flox}$	Gift from Dr. Keiko Nonomura	Cahalan et al.[40]
Mouse: NeuroD1-Cre	MMRRC at UC Davis	StockTg (Neurod1-cre) RZ24Gsat/Mmucd; RRID:MMRRC_036320-UCD
Mouse: *PIEZO1*-tdTomato	Gift from Dr. Keiko Nonomura	Koser et al.[41]
Oligonucleotides		
Forward primer for *PIEZO1*^{flox} 5′CTTGACC TGTCCCCTTCCCCATCAAG3′	Eurofins Genomics	N/A
Reverse primer-1 for *PIEZO1*^{flox} 5′AGGTT GCAGGGTGGCATGGCTCTTTTT3′	Eurofins Genomics	N/A
Reverse primer-2 for *PIEZO1*^{flox} 5′CAGTC ACTGCTCTTAACCATTGAGCCATCTC3′	Eurofins Genomics	N/A
Forward primer for NeuroD1-Cre^{cre} 5′ TAGGATTAGGGAGAGGGAGCTGAA 3′	Eurofins Genomics	N/A
Reverse primer for NeuroD1-Cre^{cre} 5′ CGGCAAACGGACAGAAGCATT 3′	Eurofins Genomics	N/A
Forward primer for Tdt-WT 5′GACAGGA TTGTGGGGCTGTACGTC3′	Eurofins Genomics	N/A
Reverse primer for Tdt-WT 5′GCAGCTA CACTCCAACCCAAGGAG3′	Eurofins Genomics	N/A
Forward primer for Tdt-KI 5′CACCTGTT CCTGTACGGCATGGAC3′	Eurofins Genomics	N/A

(*Continued on next page*)

Continued

REAGENT or RESOURCE	SOURCE	IDENTIFIER
Mm-Piezo1-O1(*in situ* hybridization probe)	Advanced Cell Diagnostics	Cat No: 500511 LOT: 19100A
DapB(*in situ* hybridization probe)	Advanced Cell Diagnostics	Cat No: 310043 LOT: 2005245
Recombinant DNA		
Plasmid: pCAG-MRLC-2GFP	This paper	N/A
Plasmid: pCAG-ezrin-GFP	This paper	N/A
Plasmid: pCAG-lifeact-2xGFP	Wu et al.[31]	N/A
Plasmid: pCAG-lifeact-tdTomato	This paper	N/A
Plasmid: pCAG-mScarlet-NLS	This paper	N/A
Plasmid: pCAGplay-GCaMP6s	gift from Dr. Yoshiaki Tagawa	N/A
Software and algorithms		
Fiji (ImageJ 2.0)	http://fiji.sc	RRID:SCR_002285
Python 3	https://github.com/rcsb/mmtf-python	RRID:SCR_024120
GraphPad Prism 9	http://www.graphpad.com/	RRID:SCR_002798
R software	http://www.r-project.org/	RRID:SCR_001905
Other		
33-gauge needle	ITO	MS-NE05 33G 20-10-90
Tweezer-type electrode	Nepagene	CUY650P3
electroporator CUY21	Nepagene	CUY21
Vibratome(*Neo* linear Slicer AT)	DOSAKA EM CO,.LTD	NLS-AT
Millicell-CM	Millipore	PICM0RG50
glass-bottom 35-mm culture plates	Iwaki	3910–035
6.5 mm Transwell Permeable Supports(3-μm-pore)	Corning	No.3415
6.5 mm Transwell Permeable Supports(8-μm -pore)	Corning	No.3422
Sylgard 184 Silicone elastomer kit (Polydimethylsiloxane:PDMS)	Dow Corning	98–0898
fluoro-silane(Trichloro-perfluoro silane)	Sigma Aldrich	448931-10G
3 mm diameter circular puncher	Ted Pella	15111–30 Biopunch
60-mm cultured plate	Iwaki	3010–060
4-20% Mini-PROTEAN TGX gel	Bio-Rad	4561094
PVDF membrane	Millipore	IPFL00005
OCT compound	Sakura Finetek Japan	4583
Super frost slide glasses	Matusnami Glass IND., LTD	S9115
ChemiDoc XRS+ System	Bio-Rad	1708265
BX61WI	Olympus	N/A
FV1000	Olympus	N/A
GaAsP detector	Olympus	FV12-MHSY(F)
60× water-immersion objective	Olympus	LUMPlanFI/IR 60XW
100× oil-immersion objective	Olympus	UPLSAPO100XO
spinning-disk confocal microscope CV1000	Yokogawa	N/A
Dragonfly High Speed Confocal Microscopy System	Andor	N/A
epifluorescent inverted microscope IX83	Olympus	N/A
spinning-disk confocal microscope CSU-W1	Yokogawa	N/A
LDI-7	89 North	N/A
iXon3 885	Andor	N/A

(*Continued on next page*)

Continued

REAGENT or RESOURCE	SOURCE	IDENTIFIER
cryostat	Leica	CM1950
RNAscope 2.5HD Detection Reagents-RED	ACD	322360
BioAnalyzer	Agilent Technologies	N/A
Illumina NextSeq 500 system	Illumina	N/A
AZ5214E (photoresist)	Merck Performance Materials Pte Ltd, Singapore	N/A
AZ 400K (developer)	Merck Performance Materials Pte Ltd, Singapore	N/A
O_2, CF_4, C_4F_8, SF_6 (Process Gases, 99.9995% purified)	Air Liquide Singapore PTE ltd	N/A

EXPERIMENTAL MODEL AND STUDY PARTICIPANT DETAILS

Animal models

Mice were handled in accordance with the guidelines of the Animal Experiment Committee of Kyoto University. Timed-pregnant ICR females were purchased from Japan SLC. *PIEZO1*$^{flox/flox}$ mice were generated as previously described.[40] NeuroD1-Cre mice were obtained from MMRRC at UC Davis [StockTg (Neurod1-cre)RZ24Gsat/Mmucd] and backcrossed to the C57BL/6 strain. Postmitotic neuron-specific PIEZO1 mutant mice were obtained by crossing *PIEZO1*$^{+/flox}$ mice with NeuroD1-Cre$^{+/Cre}$ mice, and littermates derived from *PIEZO1*$^{flox/flox}$ and *PIEZO1*$^{flox/flox}$; NeuroD1-Cre$^{+/Cre}$ mice on the pure C57BL/6 genetic background were used for subsequent studies. Newborn homozygous floxed PIEZO1 littermates were genotyped for presence or lack of NeuroD1-Cre either on postnatal day 4–5 for use in primary cultures or immunohistochemistry experiments. Piezo1 tdTomato mice were described previously.[42] No distinction between male and female pups were made for experiments. Mice were kept in a 12 h dark/light cycle at 23 ± 3°C/50% humidity in standard SPF housing.

Reagents

Chemicals and the working concentrations used in the pharmacological assays are as follows: blebbistatin (Sigma, B0560, 50 μM), cytochalasin D (TOCRIS, 1233, 10 μM), latrunculin B (KOM, AG-CN2-0031-M001, 1 μM), jasplakinolide (CALBIOCHEM, 420107, 5 μM), GsMTx4 (Abcam, ab141871, 10 μM), SKF96365 (CALBIOCHEM, 567310, 100 μM), HC-067047 (Millipore, 616521, 1 μM), Rho inhibitor 1 (Cytoskeleton, CT04, 0.1 μg/mL), NSC23766 (CALBIOCHEM, 553502, 50 μM), Yoda1 (Sigma, SML1558, 100 μM), Dooku1 (TOCRIS, 6568, 100 μM), BAPTA, extracellular calcium chelator (Abcam, ab144924, 5 μM), EGTA (ThermoFisher, E1219, 100 μM), thapsigargin (Abcam, ab120286, 2 μM), Gö6983 (CALBIOCHEM, 365251, 1 μM), LY333531 (Enzo, ALX-270-348, 10 μM), and NSC668394 (Millipore, 341216, 10 μM).

Genotyping

Tail clippings were digested in 50 mM NaOH for 10 min at 95°C. Each alleles were identified using primers as below; The *PIEZO1*^{flox} allele: 5′CTTGACCTGTCCCCTTCCCCATCAAG3′, 5′AGGTTGCAGGGTGGCATGGCTCTTTTT3′ and 5′CAGTCACTGCTCTTAA CCATTGAGCCATCTC3’; NeuroD1-Cre^{cre} allele: 5′ TAGGATTAGGGAGAGGGAGCTGAA 3′ and 5′ CGGCAAACGGACAGAAGC ATT 3’; PIEZO1-tdTomato allele: 5′GACAGGATTGTGGGGCTGTACGTC3′, 5′GCAGCTACACTCCAACCCAAGGAG3′ and 5′CACCT GTTCCTGTACGGCATGGAC3′ respectively. Each DNA fragment was amplified by KOD FX polymerase kit (Toyobo).

METHOD DETAILS

In vivo electroporation and image acquisition

P7 or P8 mice were anesthetized on ice and injected with plasmid DNAs diluted in Tris-EDTA buffer with a 33-gauge needle connected to the anode. Tweezer-type electrodes connected to the cathode were placed on the occipital regions. Six electric pulses of 70 mV for 50 ms duration were applied with 150 ms intervals using CUY21 (Nepagene). The pups were revived at 37°C and returned to the litter. Two days after electroporation, cerebella were removed and embedded in 3.5% agarose and sectioned into 300 μm-thick coronal slices with a vibratome. Slices placed on Millicell-CM (Millipore) were mounted in collagen gel and soaked in the media (60% BME, 25% Earle’s balanced salt, 15% horse serum, 3 mM L-glutamine, 1 mM sodium pyruvate, 5.6 g/L glucose, 1.8 g/L sodium bicarbonate, 1x *N*-2 supplement). The tissue was kept in an incubator chamber attached to an upright microscope stage BX61WI (Olympus) at 37°C with 85% O_2/5% CO_2 flow. Images were obtained with FV1000 equipped with a confocal GaAsP detector every 5 min through a 60× water-immersion objective (N.A. 1.1).

Matrigel culture

For primary CGN cultures, cerebella from postnatal day 4–6 mouse littermates of both sexes were dissected in HBSS (Gibco), pooled together, and dissociated using the Neuron Dissociation Kit (Wako Pure Chemical Industries, Ltd). Dissociated neurons were transfected with 6 μg of plasmid DNAs by using lipofectamine 2000 (Thermo Fisher Scientific) according to the manufacturer's instruction. Transfected cells were incubated in non-coated dishes for 8 h to make cell aggregates. For 3D cultures, resultant aggregates were suspended in 60% Matrigel (Growth Factor Reduced, Corning) in the medium (BME with 26.4 mM D-glucose, 25 mM sodium bicarbonate, 1% bovine serum albumin, 1x *N*-2 supplement and Penicillin-Streptomycin) and plated in glass-bottom 35-mm culture plates (Iwaki) and then incubated at 37°C for 30 min to allow a gel to form. Each well was then flooded with the culture medium. For 2D cultures, 60% Matrigel was plated into glass-bottom plates and solidified at 37°C for 30 min. Reaggregates were suspended in the culture medium and plated on top of the gel layer. Neurons were incubated in 37°C/5% CO_2 for 24h and subjected for live-cell imaging.

Interneurons were prepared from the medial ganglionic eminence (MGE) of embryonic day 14.5 mice and dissociated in 0.04% trypsin in HBSS/0.65% Glucose as described in Sawada et al.[66] Dissociated interneurons were subjected for transfection and Matrigel culture as described above.

Transwell assay

Dissociated CGNs were transferred in culture medium to the upper compartment of 3-μm-pore or 8-μm-pore polycarbonate membrane inserts (6.5 mm Transwell Permeable Supports cat. No. 3415 and 3422, Corning) coated with poly-*d*-lysine and laminin at 2.9 x 10^4 cells/well. Cells were allowed to transmigrate toward the lower compartment for 6 h in the presence or absence of indicated drugs. Transmigration efficiency was calculated as number of cells at the lower compartment divided by the number of cells added to the upper compartment of a transwell. Each drug for pharmacological inhibition was added to the top of the membrane 2 h after cell spreading for cell attachment.

Plasmids

To generate pCAG-MRLC-2GFP constructs, mouse MRLC cDNA from a mouse brain cDNA library fused with tandemly duplicated EGFP at the C terminus. MRLC-2GFP was inserted into pCAGGS vector as described previously.[31] As for pCAG-ezrin-GFP constructs, mouse ezrin cDNA from a mouse brain cDNA library was recombined into pENTR1A. In parallel, the gateway cassette from pDest-eGFP-N1[67] was recombined into pCAGGS to generate pCAG-Dest-eGFP. To generate pCAG-ezrin-GFP, mouse ezrin cDNA in pENTR1A was recombined into pCAG-Dest-eGFP by LR recombination using Gateway cloning vectors with Gateway LR Clonase II Enzyme Mix (Invitrogen) as previously described.[67] pCAG-lifeact-tdTomato was created by insertion of the lifeact sequence fused with tdTomato sequence into pCAGGS vector. As for mScarlet-NLS, mScarlet sequence (addgene #85042, a gift from Dorus Gadella, University of Amsterdam) fused with nuclear localization sequence (NLS) as described previously.[67]

Microfabrication-based devices

Microfluidic devices were fabricated in Polydimethylsiloxane (PDMS) using soft-lithographic procedures. A primary silicon mold with etched features (5 and 35 μm respectively for channels and expansion chambers) was prepared using 2 steps Reactive Ion Etching and aligned photolithography for patterning. PDMS, Sylgard 184 from Dow Corning, was prepared mixing the base resin and the reticulation agent in a 10:1 ratio. After vacuum degassing for about 30 min to remove all trapped air, the PDMS was poured on the silicon mold and cured for 1 h at 70°C on a hot plate. This PDMS first replica was then coated with a fluoro-silane (Trichloro-perfluoro silane, Sigma Aldrich 448931-10G) as an anti-sticking layer and used to produce the final devices in PDMS by cast molding: Sylgard 184 was mixed in a 10:1 ratio with reticulation agent and degassed, then poured on the PDMS mold an thermally cured for 1 h at 70°C. The cured PDMS was then peeled-off the PDMS mold, and devices were diced by cutting using a razor blade. In- and Out-let point were punched through the PDMS with a 3 mm diameter circular puncher (Ted Pella, 15111-30 Biopunch), and finally each device was sealed to a glass coverslip using plasma activation of PDMS and glass surfaces to promote the chemical bonding. More detailed protocol is described below (Steps I-X).

First lithography step

We used 4″, single-side polished (100) prime Si wafers with 300 nm thick thermally grown SiO_2 wafers for the fabrication of the master mold.

A 1.5 μm thick layer of positive tone photo-resist (AZ5214E) is deposited on the polished side of the wafer by spin-coating at 2500 rpm for 45 s. After spin-coating, a pre-bake is applied to remove the excess of solvent (90 s at 110°C on a Hot Plate). The photo-resist is then exposed to UV light through an optical mask with the pattern of the final device (about 100 mJ/cm^2 energy dose, UV photons at 365 nm generated by a 500 W Xe-Hg arc lamp) and developed to reveal the exposed image by immersion in AZ 400K developer diluted 1:4 in DI water for 40 s. After rinsing with clean DI water and drying with blowing N_2 gas, the wafer is ready for the next step.

Oxide layer dry etching

The 300 nm thick oxide layer is etched in a Reactive Ion Etching chamber using the patterned photo-resist as a mask. We used a Samco RIE-10NR tool for the silicon oxide etching with the following process parameters: 150 W power (source at 13.56 MHz), gas mixture of CF_4 (40 sccm) and O_2 (4 sccm) at a chamber pressure of 15 Pa; this process has an etching rate of approx.

100 nm/min in SiO_2, thus we applied the process for 3 min 15 s where the small excess of time is to make sure the oxide layer is fully removed from the exposed areas.

Residual photo-resist removal

The photo-resist remaining after the oxide etching is completely removed and the wafer is cleaned in two steps; first the wafer is kept in a bath of Acetone for 5 min with gentle agitation, then the wafer is moved in two a bath of Isopropyl alcohol and washed there for 30 s, finally the wafer is removed from the bath and rinsed with N_2 blow gun. The second and final cleaning step is an O_2 plasma process which we carried in a Diener Pico plasma tool, with 20 sccm O_2 flow, the chamber is kept at 2 mbar pressure and a power of 90 W is applied to the gas to generate the plasma for 2 min.

Second lithography

On the cleaned wafer, AZ5214E photo-resist is coated in the same way as in step 1, then lithography is done with a different optical mask with the second lay-out. The lithographic process is exactly the same as in step 1, the patterned photo-resist will leave exposed only selected portions of the previous pattern etched in the silicon oxide layer.

First deep silicon etching

In this step, the wafer as prepared after step 3 is placed in the reactor of an Inductively Coupled Plasma machine (ICP) for a first step of deep silicon etching. Silicon etching in an ICP is capable of producing vertical profiles with etching depth up to several tens of μm. We used a BOSH-like process, which works with alternating a coating step with an etching one, resulting in vertical pattern transfer. The processes for the two steps are, respectively.

(1) Coating step: C_4F_8 (140 sccm) is fluxed in the vacuum chamber kept at a pressure of 6 Pa and 500 W of power (source at 13.56 MHz) is applied to generate the plasma for a duration of 6 s. The plasma in this step produces a thin teflon-like conformal coating on the wafer
(2) Etching step: SF_6 (130 sccm) and O_2 (13 sccm) gas mixture is fluxed in the vacuum reactor chamber kept at 8 Pa of pressure and 500 W of power (source at 13.56 MHz) is applied to generate the plasma for a duration of 8 s. The plasma in this step produces reactive species which remove the thin protective coating generated in the step a more efficiently on the horizontal surfaces and then chemically remove Si where exposed

This etching process in our Sentech 500Si ICP reactor produces an etching rate in Si of approximately 250 nm/cycle (1 cycle: 1 coating step followed by 1 etching step). In this first silicon etching step we reached a final etching depth of 30 μm (120 total cycles)

Photo-resist removal

After the first silicon etching, the wafer is removed from the ICP and the residual photo-resist mask is cleaned similarly to step 3. At this stage, we confirmed the etched depth in the silicon with a Bruker Stylus profiler.

Second and final silicon etching

The wafer after step 5 is placed back in the same ICP reactor, and the same process is applied to etch extra 5 μm in the Si (20 cycles). The previous feature will results finally in a 35 μm deep cavity, while the feature exposed for the first time will have a final etch depth of 5 μm.

Silanization

The wafer after step 6 is patterned with features etched down to a final depth of 35 and 5 μm. This wafer is now considered as the Master Mold for replica molding with PDMS. In this step the mold is treated with an anti-sticking coating by vapour-deposition of a molecular layer of Trichloro (1H,1H,2H,2H-perfluorooctyl) silane. First, the surface of the mold is activated with a 30 s O_2 plasma (Pico Diener plasma tool, O_2 20 sccm with the chamber at 2 mbar pressure, 90 W RF power at 13.56 MHz) then immediately placed in a plastic vacuum jar together with a small drop of perfluorosilane (approx. 20 μL) and kept in vacuum (1 mbar or less) for at least 1 h. After at least 1 h, the wafer can be retrieved from the vacuum jar and it is ready to be used for PDMS casting multiple times.

PDMS replica

Sylgard 184 PDMS is prepared by mixing the silicone elastomer with its curing agent in a 10:1 ratio (in weight, prepare about 25 g total). After mixing, degas in a vacuum jar (approx. 1 mbar) for about 30 min, or until no more visible air bubbles are visible.

Place the silanized master mold in a Petri dish and slowly pour the degassed PDMS until the master if completely covered. Place the Petri dish containing the master mold covered with PDMS in the vacuum jar and degas at 1 mbar or lower for 5-10 min to ensure no air is trapped at the surface of the mold.

Place the Petri dish with the mold and the PDMS on a hot plate at 70°C or in an oven at 70°C an allow for the PDMS to thermally cure for about 1.5 h. After thermal curing is done, with a blade carefully cut around the edge of the mold then slowly peel-off the cut section of cured PDMS from the mold (which is left in the Petri dish). Store the PDMS cut in a second Petri dish; the master mold can be kept in its Petri dish surrounded by cured PDMS and protected with the Petri dish lid. The silicon master mold can be re-used for multiple steps of replica molding.

PDMS working mold preparation

The PDMS replica of the master mold prepared in step 8 is now patterned with protrusion that replicate exactly, the features in the master mold (with inverted polarity). This PDMS replicas can be used as a Working Mold to produce by a second step of PDMS replica molding the final devices. Prior to PDMS casting on the Working Mold, it needs to be coated with the same anti-sticking layer as in step 7. The process is identical, except the O_2 plasma is carried on at lower power (30 W).

Live-cell imaging

2D and 3D Matrigel cultures and dissociated CGNs on micropatterned substrates coated with laminin were observed with a spinning-disk confocal microscope CV1000 (Yokogawa) through a 20× objective (N.A. 0.75) or a 100× oil-immersion objective (N.A. 1.3) or a 60× water-immersion objective (N.A. 1.2), or with Dragonfly High Speed Confocal Microscopy System (Andor) through a 100× oil-immersion objective (N.A. 1.4), or an inverted microscope IX83 (Olympus) combined with a spinning-disk confocal system (CSU-W1(Yokogawa), LDI-7(89 North), iXon3 885 (Andor)) through 100× oil-immersion objective (N.A. 1.4) at 37°C with 5% CO_2 flow. For Ca^{2+} imaging, the CGNs transfected with GCaMP6s were observed with an epifluorescent inverted microscope IX83 (Olympus) through a 100× oil-immersion objective (N.A. 1.3) or with a spinning-disk confocal microscope CV1000 (Yokogawa) through a 60× water-immersion objective (N.A. 1.2).

Westernblotting

Dissociated CGNs were plated in 60-mm cultured plates (Iwaki) coated with poly-*d*-lysine and laminin and maintained for 12 h in culture medium at 37°C/5% CO_2. LY333531 was added to cultures for 1 h at a final concentration of 10 μM before treatment with Yoda1. Yoda1 (Sigma) was added to cultures for 5 min at a final concentration of 100 μM. Equivalent volumes of solvent were added to control cultures. Cultures were washed with cold PBS and lysed in RIPA buffer (50 mmol/L Tris-HCl (pH 7.6), 150 mmol/L NaCl, 1% NP40, 0.5% Sodium Deoxycholate, 0.1% SDS) with Protease inhibitor cocktail (EDTA free) (Nacalai) and Phosphatase inhibitor cocktail (Sigma). Lysates were incubated at 4°C for 15 min and cleared at 15,000 × *g* for 15 min at 4°C. Total protein was normalized using Protein assay BCA kit (Nacalai). Equal amounts of lysates were separated by SDS-PAGE in 4–20% Mini-PROTEAN TGX gel and transferred onto PVDF membrane (Millipore). Membranes were blocked for 60 min at room temperature in PBS-Tween with 5% skimmed powder milk. Membranes were incubated with primary antibodies in blocking buffer overnight at 4°C at the following concentrations: anti-Ezrin (mouse, 1: 1/1000; Abcam), anti-phospho T567 Ezrin (rabbit, 1: 1/300; Abcam) and anti-GAPDH (mouse, 1: 1/2000; Abcam). Membranes were washed and incubated for 30 min in blocking buffer containing HRP-conjugated anti-rabbit or mouse secondary antibodies (1:10000; Bio-Rad). Signal was detected with ECL Prime (G.E. Healthcare) and imaged on a ChemiDoc XRS+ System (Bio-rad). *p*-Ezrin intensity was normalized by total Ezrin intensity and compared using replicates from 3 independent experiments.

BrdU pulse-labeling

5-bromo-2′-deoxyuridine (BrdU, Invitrogen) was dissolved in PBS. Wildtype and PIEZO1 conditional knockout mice at P9 were injected i.p. with BrdU (15 mg/kg) for labeling. Immunofluorescence and BrdU detection were done at P13.

Immunofluorescence

Mice were deeply anesthetized by isoflurane, and were transcardially perfused with phosphate buffer (PB) followed by 4% paraformaldehyde (PFA) in PB. Brains were removed and postfixed overnight in 4% PFA at 4°C. Brains were then washed of PFA with three changes of 1X phosphate buffered saline (PBS), and 30% sucrose/PBS. Dehydrated brains were frozen by liquid nitrogen, then embedded into OCT compound (Sakura Finetek Japan). Sagittal sections (20 μm thick) were made using a cryostat (Leica). Slices on Super frost slide glasses (Matsunami) were treated with PBS-Triton X-100 (0.5% v/v) for 10 min, and washed with PBS-Triton X-100 (0.1% v/v). Brain slices were then blocked by incubation with 2% skim milk in PBS-Triton X-100 (0.1% v/v) for 30 min at RT. Primary antibody labeling was performed in blocking buffer overnight at 4°C as follows: anti-Pax6 (rabbit, 1:1000, Wako), anti-BrdU (mouse, 1:100, Sigma-Aldrich). After thorough washing, slices were incubated with secondary antibodies overnight at 4°C, followed by 10 μg/mL DAPI for 10 min at RT. After washing, slices were mounted with Fluoromount (DBS).

RNAscope

Fixed brains were transferred to 30% Sucrose/PBS and embedded in OCT compound. Cryosections (20 μm) were subjected to *in situ* hybridization according to the manufacturer's protocol (Advanced Cell Diagnostics, RNAscope). Probes were Mm-Piezo1-01(Cat No: 500511 LOT: 19100A) and DapB for negative control (Cat No: 310043 LOT: 2005245).

RNA-sequencing

CGNs were dissociated from 2 to 3 mouse litters at P6 and plated on laminin-coated membranes. After 8 h, RNA was extracted with a RNAeasy Mini Kit (QIAGEN) and the purity of RNA was assessed using a BioAnalyzer (Agilent Technologies). Duplicate samples were subjected for RNA-sequencing on an Illumina NextSeq 500 system using single end reads.

Quantitative image analyses and statistical analyses

Images analyses were performed using Fiji (ImageJ 2.0) or Python 3. MRLC-2GFP and ezrin-GFP signals in xy planar images resolved in 1 μm steps over the entire depth of the migrating cells were processed for maximum intensity projections. For the measurement of the intensity of cytoplasmic MRLC-2GFP, the signal intensity along a one pixel wide, 15 μm line near the midline of the cell soma was scanned in the front and rear of the nucleus. The intensity values were normalized to the average of all intensity values of each cell. The maximum intensity value obtained using the original python code were plotted for comparative analysis of data from different samples. For the measurement of the intensity of ezrin-GFP on the plasma membrane, the signal intensity on the somal plasma

membrane was scanned. The intensity values for the four subdivided areas (Front, Middle front, Middle rear, Rear) were normalized to the average of all intensity values in each cell. For quantification of $[Ca^{2+}]_i$, the average intensity of GCaMP6s signal in the soma was quantified manually in each time frame. The values were normalized to the average intensity in the soma before Yoda1 treatment.

Statistical analysis

Data were analyzed by GraphPad Prism 9 or R software.

Modeling

Simulation method

Computer simulation of a deformable spherical object that passes through a narrow tunnel was conducted based on the method of fluid–structure interaction simulation proposed in our previous studies.[68,69] A spherical object was modeled as a slightly compressible object covered with a hyperelastic membrane. For simplicity, the intracellular structures such as the nucleus were not considered. The mechanical behavior of the two-dimensional membrane was assumed to be governed by Skalak's constitutive law,[70] in which the strain energy function, W, is described using the first and second strain invariants of the right Cauchy–Green tensor, I_1 and I_2, respectively, as the following:

$$W = \frac{1}{4}G_s\left(I_1^2 + 2I_1 - 2I_2 + CI_2^2\right) \quad \text{(Equation 1)}$$

where G_s is the surface shear elastic modulus, and C is the area incompressibility coefficient. By using these two material properties, the surface Poisson's ratio, n_s, and Young's modulus, E, can be expressed using the membrane thickness, h, as $\nu_s = C/(C+1)$ and $E = 2G_s(1+\nu_s)/h$, respectively. The contraction of the membrane, which mimics actomyosin contraction at the cell membrane, was modeled by introducing the active second Piola-Kirchhoff stress tensor, $\mathbf{S}_{act}$, as

$$\mathbf{S}_{act} = A\mathbf{m}_0 \otimes \mathbf{m}_0 \quad \text{(Equation 2)}$$

where, A is the magnitude of contraction and $\boldsymbol{m}_0$ is the unit vector representing the direction of contraction in the reference state; thereby this model expresses unidirectional contraction. The membrane of the spherical object was discretized into triangular finite elements. The restoring force, $\boldsymbol{q}_{in\text{-}plane}$, acting on the membrane node $\boldsymbol{x}_m$ due to the membrane deformation was computed based on a finite element procedure.

To consider a volume constraint of the spherical object and a bending stiffness of the membrane, we introduced the Helmholtz free energies, F_{vol} and F_{bend}, respectively.[71] The free energy for the volume constraint, F_{vol}, was proposed using the object volume in the current state, V, as

$$F_{vol} = \frac{1}{2}k_{vol}\left(\frac{V}{V_0} - 1\right)^2 \quad \text{(Equation 3)}$$

where k_{vol} is the bulk modulus and V_0 is the object volume in the reference state, i.e., the volume of the undeformed sphere. Since this is an artificial free energy to model the effect of slightly compressible internal fluid, the exact value of k_{vol} is unimportant. Similarly, the bending free energy, F_{bend}, was expressed using the angle between two adjacent triangular elements (a, b) in the current state, q_{ab}, as

$$F_{bend} = \sum_{\text{adjacent } \alpha,\beta \text{ pair}} k_{bend}\left[1 - \cos\left(\theta_{\alpha\beta} - \theta_0\right)\right] \quad \text{(Equation 4)}$$

where, k_{bend} is the bending modulus and q_0 is the angle in the reference state, which was set to 0 in this study. These free energies can produce the corresponding restoring forces, q_{vol} and q_{bend}, on the membrane node $\boldsymbol{x}_m$ as the following:

$$\mathbf{q}_{vol}(\mathbf{x}_m) = -\frac{\partial F_{vol}}{\partial \mathbf{x}_m} \quad \text{(Equation 5)}$$

$$\mathbf{q}_{bend}(\mathbf{x}_m) = -\frac{\partial F_{bend}}{\partial \mathbf{x}_m} \quad \text{(Equation 6)}$$

Additionally, by considering externally applied force, $\boldsymbol{q}_{ext}$, on the membrane node $\boldsymbol{x}_m$, the total force, $\boldsymbol{q}$, acting on $\boldsymbol{x}_m$ is given by

$$\mathbf{q}(\mathbf{x}_m) = \mathbf{q}_{in-plane}(\mathbf{x}_m) + \mathbf{q}_{vol}(\mathbf{x}_m) + \mathbf{q}_{bend}(\mathbf{x}_m) + \mathbf{q}_{ext}(\mathbf{x}_m) \quad \text{(Equation 7)}$$

The proposed spherical object model was placed in a channel filled with Newtonian fluid. The fluid dynamics was numerically analyzed using the lattice Boltzmann method.[72] Furthermore, the membrane deformation of the spherical object and the surrounding fluid dynamics were coupled using the immersed boundary method.[73] In this method, the membrane force $\boldsymbol{q}$ (Equation 7) is distributed to the neighboring fluid to drive the fluid flow, and conversely, the fluid velocity determines the neighboring membrane velocity for the advection.

Simulation model

A three-dimensional model of two cylindrical channels connected by a narrow cylindrical tunnel was constructed (Figure 1G). Each channel has a diameter of 12 mm and a length of 12 mm, and the connecting tunnel has a diameter of 4 mm and a length of 4 mm. The fluid-filled space in the channels and tunnel was discretized using a three-dimensional regular lattice with an interval of 0.4 mm. The spherical object model proposed in the previous section was placed in the center of one cylindrical channel. The membrane was discretized using two-dimensional triangular finite elements with an approximately 0.2 mm edge size, which was set to be smaller than the lattice interval in the fluid-filled space to avoid leaks. To move the spherical object forward, a tensile force of 60 pN was applied uniformly on the front membrane, which is equivalent to a solid angle of 0.1 p steradian (green region shown in Figure 1G), along the longitudinal direction of the channels.

After the deformed spherical object ceased to move in the tunnel, contraction of the rear hemispherical membrane (red region shown in Figure 1G) with the magnitude of $A = 5.0\times 10^{-4}$ (Pa·m) was imposed (see Equation 2), where the direction of contraction $\boldsymbol{m}_0$ was randomly set for each triangular element within its tangential plane to represent in-plane isotropic contraction of the membrane. To verify the effectiveness of the membrane contraction to pass through the narrow tunnel, the simulation without contraction was also performed.

As boundary conditions, the no-slip condition was applied at the wall of the channels and tunnel, and the periodic boundary condition for the fluid velocity was applied at both ends of the channels. No frictional force was assumed between the wall of the tunnel and the membrane of the spherical object. The material properties of the spherical object used in the present simulation are listed below.[74,75] By using these material properties, the surface shear elastic modulus, G_s, and the surface Poisson's ratio, n_s, of the membrane can be derived as $G_s = 5.2 \times 10^{-7}$ (Pa·m) and $n_s = 0.91$, respectively.

QUANTIFICATION AND STATISTICAL ANALYSIS

Data were analyzed by GraphPad Prism 9 or R software. The number of biological replicates is indicated in the figure legend. Error bars in each graph represent the standard deviation. Statistical tests are mentioned in each figure legend. *<0.05, **$p < 0.01$, ***$p < 0.001$, ****$p < 0.0001$.